METHODS

Generation of Atg16L1-deficient mice. The fragment of the Atg16L1 gene was isolated from genomic DNA extracted from wild-type ES cells by PCR. A targeting vector was constructed by replacing exons 3, 4 and 5 of Atg16L1 with a neomycin-resistance gene cassette (neo), and a herpes simplex virus thymidine kinase driven by PGK promoter was inserted into the genomic fragment for negative selection. After the targeting vector was transfected into ES cells, G418 and gancyclovir doubly resistant colonies were selected and screened by PCR and Southern blotting. Homologous recombinants were micro-injected into C57BL/6 female mice, and heterozygous F1 progenies were intercrossed in order to obtain Atg16L1-deficient (Δ/Δ) mice. The Atg16L1-deficient mice used were on a 129Sv × C57BL/6 background.

For the generation of fetal liver chimaeric mice, fetal liver cells were harvested at E15.5 and injected into lethally irradiated CD45.1 or C57BL6J mice. Chimaeric mice were given antibiotics in drinking water for 2 months. The mice were analysed at least 3 months after reconstitution.

Mice were maintained in our animal facility and treated in accordance with the guidelines of Osaka University.

Reagents, mice and cells. Anti-IL-1β antibodies, recombinant mouse IFN-γ, ELISA kits for mouse IL-1β, human IL-1β, mouse IL-6 and mouse TNFα, were purchased from R&D Systems. Recombinant mouse IFN-β and the ELISA kit for mouse IFN-β were purchased from PBL InterferonSource. Anti-LC3 and anti-IL-18 antibodies and the ELISA kit for IL-18 were purchased from MBL International. GM-CSF and M-CSF were purchased from Peprotech. Anti-p62/SQSTM1 antibody was purchased from BIOMOL International. Anti-Atg12, anti-phospho-IRF3, anti-phospho-p38 and anti-phospho-ERK antibodies were purchased from Cell Signaling Technology. Anti-IκBα, anti-ERK and caspase-1 p10 were purchased from Santa Cruz Biotechnology. YVAD-fmk, wortmannin and FeTPPS were purchased from Calbiochem. ATP, oxidized ATP, LPS from *Salmonella minnesota* Re 595, 3-methyadenine, muramyl dipeptide and anti-α-tubulin antibody were purchased from Sigma. Lipid A was purchased from Peptide Institute. Flagellin was purchased from Invivogen. Uric acid crystals were purchased from Alexis. N-acetyl-L-cysteine was purchased from Nacalai Tesque. Poly(I)·poly(C) was purchased from GE Healthcare. R-848 was kindly provided by the Pharmaceuticals and Biotechnology Laboratory Japan Energy Corporation. CpG oligodeoxynucleotides (ODN1668) were synthesized at Hokkaido System Science Co. Anti-Atg16L1 and anti-Atg5 antibodies were kindly donated by N. Mizushima (Tokyo Medical and Dental University).

K. pneumonia and *E. aerogenes* were kindly donated by the Research Institute of Microbial Disease, Osaka University. *E. coli* (DH5α) was purchased from TOYOBO. *Salmonella enteritica serovar typhimurium* (SR-11 × 3181) was provided by the Kitasato Institute for Life Science. Mice deficient in MyD88, TRIF or Atg7 were described previously[9,13]. Atg5-deficient MEFs and Plat-E cells were kindly donated by N. Mizushima and T. Kitamura (University of Tokyo), respectively. RAW264.7 cells were purchased from ATCC.

Plasmids. The retroviral expression constructs pMRX-ires-puro, pMRX-ires-bsr and pMRX-ires-EGFP (donated by S. Yamaoka) were derivatives of pMX (donated by T. Kitamura). Complementary DNA encoding human IL-1β was inserted into pMRX-ires-EGFP, generating pMRX-ires-IL-1β. Complementary DNA encoding Atg16L1 lacking in coiled-coil domain (Atg16L1 ΔCCDβ) was inserted into pMRX-ires-puro, generating pMRX-Atg16L1 ΔCCDβ-ires-puro. Complementary DNA encoding the GFP-Atg5 chimaeric protein was inserted into pMRX-ires-bsr, generating pMRX-GFP-Atg5-ires-bsr. Construction and inhibitory function details of pStrawberry-Atg4^{C74A} are described elsewhere[31].

RT–PCR. Total RNA was isolated using RNAeasy Mini kits (Qiagen) according to the manufacturer's instructions. Reverse transcription was performed using ReverTra Ace (TOYOBO) according to the manufacturer's instructions. For quantitative PCR, cDNA fragments were amplified by RealTime PCR Master Mix (TOYOBO) according to the manufacturer's instructions. Fluorescence from the Taqman probe for each cytokine was detected by a 7500 Real-Time PCR System (Applied Biosystems). To determine the relative induction of cytokine mRNA in response to LPS stimulation, the mRNA expression level of each cytokine was normalized to the expression level of 18S RNA. The experiments were repeated at least twice. The results were reproducible.

The primer pairs used in Supplementary Fig. 1 are as follows. Primer pair A (exon 1-2), 5′-GTTCGGCATGTCGTCGGGCCTG-3′ and 5′-ATTTCATGCC-TATTTGGCATGTCATGC-3′. Primer pair B (exon 6-7), 5′-GTCAAGCACG-GCTGCAGAAGGAGCTTG-3′ and 5′-GTAGCTGCTCTGCTGACAGCTCGG-3′. Primer pair C (exon 1-5), 5′-GTTCGGCATGTCGTCGGGCCTGN-3′ and 5′-GACCAGTTCCTGGTTCTCCTCAGTAG-3′. Primer pair D (exon 5-7), 5′-CGCCTCAATGCAGAGAATGAGAAGGAC-3′ and 5′-GTAGCTGCTCTGCT-GACAGCTCGG-3′. Primer pair E (exon 1-6), 5′-GTTCGGCATGTCGTCG-GGCCTG-3′ and 5′-CAAGCTCCTTCTGCAGCCGTGCTTGAC-3′.

Bulk protein degradation assay. Cells were exchanged into labelling medium containing ^{14}C-valine (1.5 μCi ml^{-1}) and incubated overnight. Cells were exchanged into chase medium (DMEM supplemented with 10% FBS and 10 mM unlabelled valine) and further incubated for 4 h to remove the contribution of short-lived proteins. After the chase period, cells were exchanged into HBSS containing 10 mM valine to induce autophagy. After a 2 h incubation, the media were collected and the trichloroacetic acid (TCA)-soluble fraction was analysed by scintillation counting. Cells were lysed in ice-cold RIPA buffer and the TCA-insoluble fraction was isolated and analysed by scintillation counting. To determine the rate of long-lived protein degradation, the count in the TCA-soluble fraction in the medium was divided by the equivalent TCA-insoluble count in the cell.

Detection of apoptosis. The appearance of mono/oligo-nucleosomes, markers for apoptosis, was detected by Cell Death Detection ELISA^{PLUS} (Roche). Chromatin condensation in apoptotic nuclei was detected using an ApoStrand ELISA Apoptosis Detection Kit (Biomol). The experiments were repeated twice, and the results were reproducible.

Determination of bacteria colony forming units (c.f.u.s). Levels of c.f.u.s in freshly isolated faeces or spleen were determined by homogenization of material in PBS/0.01% Triton X-100 followed by serial dilution plating on non-selective Luria-Bertani agar.

31. Fujita, N. *et al.* An Atg4B mutant hampers the lipidation of LC3 paralogues and causes defects in autophagosome closure. *Mol. Biol. Cell* advance online publication, doi:10.1091/mbc.E08-03-0312 (3 September 2008).

A New Humanized Mouse Model of Epstein-Barr Virus Infection That Reproduces Persistent Infection, Lymphoproliferative Disorder, and Cell-Mediated and Humoral Immune Responses

Misako Yajima,[1,a] Ken-Ichi Imadome,[1,a] Atsuko Nakagawa,[2] Satoru Watanabe,[3] Kazuo Terashima,[4] Hiroyuki Nakamura,[1] Mamoru Ito,[5] Norio Shimizu,[3] Mitsuo Honda,[5] Naoki Yamamoto,[4,5] and Shigeyoshi Fujiwara[1]

[1]Department of Infectious Diseases, National Research Institute for Child Health and Development, [2]Pathology Laboratory, Department of Clinical Laboratory Medicine, National Center for Child Health and Development, [3]Department of Virology, Division of Medical Science, Medical Research Institute, and [4]Department of Molecular Virology, Graduate School of Medicine, Tokyo Medical and Dental University, and [5]AIDS Research Center, National Institute of Infectious Diseases, Tokyo, and [6]Central Institute for Experimental Animals, Kawasaki, Japan

The functional human immune system, including T, B, and natural killer lymphocytes, is reconstituted in NOD/Shi-*scid*/IL-2Rγ^{null} (NOG) mice that receive hematopoietic stem cell transplants. Here, we show that these humanized mice can recapitulate key aspects of Epstein-Barr virus (EBV) infection in humans. Inoculation with $\sim 1 \times 10^3$ TD_{50} (50% transforming dose) of EBV caused B cell lymphoproliferative disorder, with histopathological findings and latent EBV gene expression remarkably similar to that in immunocompromised patients. Inoculation with a low dose of virus ($\leq 1 \times 10^1$ TD_{50}), in contrast, resulted in apparently asymptomatic persistent infection. Levels of activated $CD8^+$ T cells increased dramatically in the peripheral blood of infected mice, and enzyme-linked immunospot assay and flow cytometry demonstrated an EBV-specific T cell response. Immunoglobulin M antibody specific to the EBV-encoded protein BFRF3 was detected in serum from infected mice. The NOG mouse is the most comprehensive small-animal model of EBV infection described to date and should facilitate studies of the pathogenesis, prevention, and treatment of EBV infection.

Epstein-Barr virus (EBV) is a tumor virus associated with a variety of malignancies, including Burkitt lymphoma, nasopharyngeal carcinoma, and Hodgkin lymphoma [1]. It is also an etiological agent of infectious mononucleosis (IM), which is characterized by transient proliferation of EBV-infected B lymphoblastoid cells and an excessive anti-EBV T cell response. EBV has a unique ability to growth transform human B lymphocytes in vitro and establish lymphoblastoid cell lines (LCLs) [2]. EBV-transformed lymphoblasts express 6 nuclear proteins (Epstein-Barr nuclear antigen [EBNA] 1, 2, 3A, 3B, 3C, and LP) and 3 membrane proteins (latent membrane protein [LMP] 1, 2A, and 2B), and this pattern of EBV gene expression is termed latency III. In contrast, Burkitt lymphoma cells express only EBNA1 consistently (latency I), whereas Hodgkin lymphoma and nasopharyngeal carcinoma cells express EBNA1, LMP1, and LMP2 (latency II). In vivo, EBV-transformed cells are effectively removed by virus-specific cytotoxic T cells, and EBV infection in immunocompetent humans is usually subclinical, except for IM caused by primary infection during adolescence or adulthood. However, in immunocompromised hosts, such as patients with AIDS and transplant recipients, EBV-infected B lymphoblasts can proliferate and cause lymphoproliferative disorder.

Received 28 December 2007; accepted 19 March 2008; electronically published 15 July 2008.

Potential conflicts of interest: none reported.

Financial support: Ministry of Health, Labour, and Welfare of Japan (grants H18-Shinko-013 and H19-AIDS-003).

* M.Y. and K.-I.I. contributed equally to this study.

Reprints or correspondence: Dr. Shigeyoshi Fujiwara, Dept. of Infectious Diseases, National Research Institute for Child Health and Development, 2-10-1 Okura, Setagaya-ku, Tokyo 157-8535, Japan (shige@nch.go.jp); or, Dr. Norio Shimizu, Dept. of Virology, Div. of Medical Science, Medical Research Institute, Tokyo Medical and Dental University, 1-5-45 Yushima, Bunkyo-ku, Tokyo 113-8519, Japan (nshivir@tmd.ac.jp); or, Dr. Naoki Yamamoto, AIDS Research Center, National Institute of Infectious Diseases, 1-23-1 Toyama, Shinjuku-ku, Tokyo 162-8640, Japan (nyama@nih.go.jp).

The Journal of Infectious Diseases 2008; 198:673–82

0022-1899/2008/19805-0008$15.00

DOI: 10.1086/590502

EBV infects only humans in nature and limited animal species under experimental conditions. It can infect cotton-top tamarins and induce lymphomas, which have been used as a model of EBV-associated lymphomas [3, 4]. Nonhuman primates possess their own lymphocryptoviruses related to EBV, and research on the use of these virus-host systems as models of EBV infection is currently in progress [5, 6]. Small-animal models of EBV have also been developed, which are particularly useful when a large number of animals are necessary. *Scid* mice that receive intraperitoneal transplants of EBV-transformed LCLs or peripheral blood mononuclear cells (PBMCs) isolated from EBV-infected persons develop lymphomas, which have been used as a model of human lymphoproliferative disorder [7–9]. Recently, NOD/*scid* mice transplanted with human hematopoietic stem cells (HSCs) and reconstituted mainly with B lymphocytes were infected with EBV, and the development of lymphoproliferative disorder was described [10]. The immune response to EBV was not studied in these *scid* or NOD/*scid* mouse models. Very recently, a functional human immune system could be reconstituted in highly immunodeficient mouse strains, and these so-called humanized mice were shown able to mount an EBV-specific T cell response [11, 12]. These studies were, however, performed mainly using immunological standpoints and did not provide detailed virological data.

NOD/Shi-*scid*/IL-2Rγ^{null} (referred to here as NOG) is a highly immunodeficient mouse strain that was developed very recently and that, after transplantation with cord blood HSCs, is able to reconstitute most major components of the hematolymphoid system, including T cells, B cells, NK cells, macrophages, and dendritic cells [13–15]. Human T cells that develop in NOG mice are functional in that they can be activated to display cytotoxic activity [15, 16]. These properties made NOG mice an excellent model of human virus infections targeting the immune system, such as those with human T-lymphotropic virus–1 and HIV-1 [17–20]. Here, we provide evidence that humanized NOG mice can reproduce various key aspects of human EBV infection and propose that they may be a valuable tool for studies of EBV infection.

Table 1. Primers for reverse-transcription polymerase chain reaction to detect Epstein-Barr virus (EBV) transcripts.

Transcript, primer	Sequence (5'→3')
EBNA1	
5'	gatgagcgtttgggagagctgattctgca
3'	tcctcgtccatggttatcac
EBNA2	
5'	agaggaggtggtaagcggttc
3'	tgacgggtttccaagactatcc
LMP1	
5'	ctctccttctcctcctcttg
3'	caggagggtgatcatcagta
LMP2A	
5'	atgactcatctcaacacata
3'	catgttaggcaaattgcaaa
LMP2B	
5'	cagtgtaatctgcacaaaga
3'	catgttaggcaaattgcaaa
EBER1	
5'	agcacctacgctgccctaga
3'	aaaacatgcggaccaccagc
BZLF1 (first)	
5'	attgcaccttgccgccaccttg
3'	cgcattttctggaagccacccga
BZLF1 (second)	
5'	gaccaagctaccagagtctat
3'	cagaatcgcattcctccagcga
BMRF1	
5'	ctagccgtcctgtccaagtgc
3'	agccaaacagctccttgccca
BLLF1	
5'	gtcagtacaccatccagagcc
3'	ttggtagacagccttcgtatg
GAPDH	
5'	gcctcctgcaccaccaactg
3'	cgacgcctgcttcaccaccctct

NOTE. EBNA, Epstein-Barr nuclear antigen; EBER, EBV-encoded small RNA; LMP, latent membrane protein.

METHODS

Preparation of humanized mice. NOG mice were obtained from the Central Institute for Experimental Animals (Kawasaki, Japan). Protocols for experiments with NOG mice were approved by the Institutional Animal Care and Use Committee of the National Institute of Infectious Diseases (NIID). Cord blood was supplied by the Tokyo Cord Blood Bank after obtaining informed consent. The use of human materials in this research was approved by the institutional review boards of the National Research Institute for Child Health and Development, the NIID, the Tokyo Medical and Dental University, and the Tokyo Cord Blood Bank. The isolation of human CD34$^+$ HSCs from cord blood by means of the MACS Direct CD34 Progenitor Cell Isolation Kit (Miltenyi Biotec), their intravenous injection (1×10^4 to 1.2×10^5 cells/mouse) into 6–10-week-old female NOG mice, and the characterization of the reconstitution of the human hematoimmune system were done as described elsewhere [18, 20]. NOG mice in which the human hematoimmune system was reconstituted are referred here as humanized NOG (hNOG) mice.

Experimental EBV infection, quantification of viral DNA, and detection of viral mRNAs. Virus production by EBV-infected Akata cells was stimulated by brief treatment with anti-IgG antibody (Dako), and culture fluid was used as inoculum after filtration through a 0.45-μm membrane filter [21]. For virus titration, cord blood lymphocytes were plated at the density

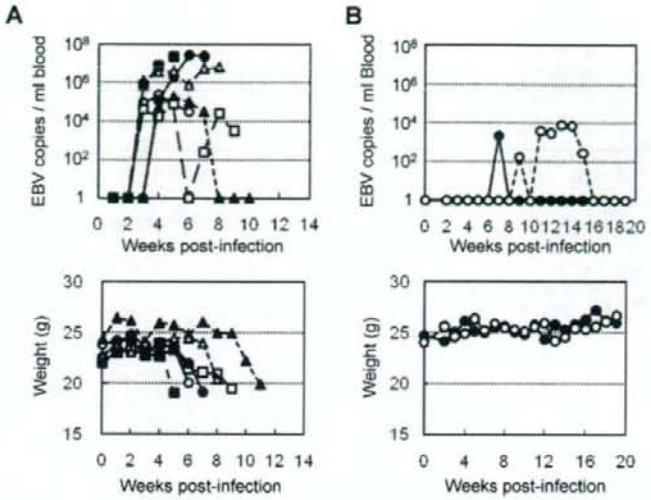

Figure 1. Peripheral blood Epstein-Barr virus (EBV) DNA load and body weight in humanized NOG (hNOG) mice infected with EBV. *A*, Infection at a high dose of virus. Six mice were inoculated intravenously with 1×10^3 TD_{50} of EBV. Peripheral blood EBV DNA load *(upper panels)* and body weight *(lower panels)* were then determined weekly. Each symbol in the graphs represents an individual mouse. Interruption of records indicates the death or killing of a mouse. *B*, Infection at lower doses. Peripheral blood EBV DNA load *(upper panel)* and body weight *(lower panel)* of 2 mice inoculated with low doses of EBV (*black circle*, 1×10^{-1} TD_{50}; *white circle*, 1×10^{1} TD_{50}) are shown.

of 2×10^5 cells per well in 6-well plates and then inoculated with serial 10-fold dilutions of virus preparation. The number of wells with proliferating lymphocytes was counted 6 weeks after infection, and the titer of the virus in 50% transforming dose (TD_{50}) was determined by the Reed-Muench method [22]. EBV was inoculated intravenously through the tail vein. EBV DNA was quantified by a real-time quantitative polymerase chain reaction (PCR) assay based on the TaqMan system (Applied Biosystems), as described elsewhere [23]. Analysis of EBV gene expression by reverse-transcription PCR (RT-PCR) was done as described elsewhere, using the primers listed in table 1 [24].

Histopathology, in situ hybridization (ISH), and immunohistochemistry. Tissue samples were fixed in 10% buffered formalin, embedded in paraffin, and stained with hematoxylin-eosin. For phenotypic analysis of proliferating lymphocytes, immunostaining for CD3 (Nichirei), CD4 (Novocastra), CD8 (Nichirei), CD45RO, CD20, CD79a, CD30, Mum1 (Dako), CD23, CD10, CD56 (Novocastra), granzyme B (Dako), and T cell intracellular antigen 1 (Beckman Coulter) was performed on paraffin sections. EBV was detected by immunostaining for LMP1 and EBNA2 (Dako) and by ISH with EBV-encoded small RNA (EBER) probe. Immunohistochemistry and ISH were performed on an automated stainer (Benchmark XT; Ventana Medical Systems), in accordance with the manufacturer's recommendations. To determine the cell lineage of EBV-infected cells, paraffin sections were applied to double staining with EBER ISH and immunohistochemistry.

Detection of EBV-specific T cell response. Enzyme-linked immunospot (ELISPOT) assay was performed with the Immunocyto IFN-γ ELISPOT Kit (MBL), in accordance with the instructions supplied by the manufacturer. Briefly, $CD8^+$ T cells were isolated from PBMCs from EBV-infected hNOG mice with the IMag anti-human CD8 Particles–DM (BD Biosciences). Mixture of these $CD8^+$ T cells and an autologous LCL were incubated with interleukin (IL)–2 in microplates coated with antibody to interferon (IFN)–γ for 17 h. Captured IFN-γ was detected by use of biotinated antibody to IFN-γ and alkaline phosphatase–conjugated streptavidin and was visualized by reaction with the BCIP/NBT chromogen substrate. The unpaired Student's *t* test was used for statistical analysis. IFN-γ secretion in response to EBV was also examined by flow cytometry, as described elsewhere [25]. Briefly, aliquots of murine splenocytes and an LCL were mixed in 6-well plates in the presence of brefeldin A (10 μg/mL) and incubated at 37°C in 5% CO_2 for 17 h. After incubation, the cell suspensions were stained with phycoerythrin-conjugated anti-human CD69, phycoerythrin–Texas red–conjugated anti-human CD45, and phycoerythrin–cyanin 5–conjugated anti-human CD8 for 30 min at 4°C and were fixed with 2% paraformaldehyde. Cells were then permeabilized and stained with BD Perm/Wash buffer (BD Biosciences) containing fluorescein isothiocyanate–conjugated anti-human IFN-γ for 30 min at 4°C. Stained cells were analyzed using an EpicsXL flow cytometer (Beckman Coulter).

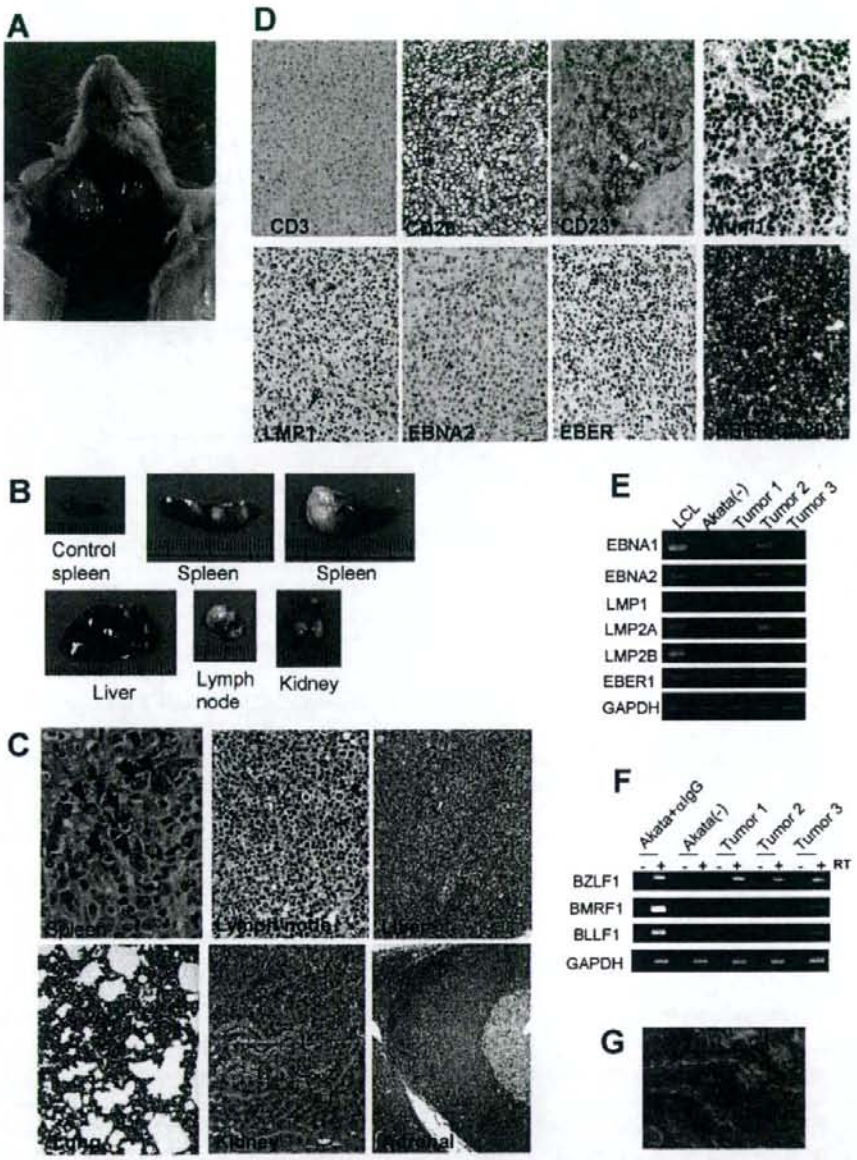

Figure 2. Pathological and virological analyses of Epstein-Barr virus (EBV)–infected humanized NOG (hNOG) mice. *A*, Photograph of an EBV-infected mouse showing tumors in the cervical area. *B*, Photographs of spleens, liver, lymph node, and kidney from EBV-infected mice with lymphoproliferative disorder. The upper left panel shows the spleen from an uninfected mouse. *C*, Photomicrographs of hematoxylin-eosin–stained tissues from mice with lymphoproliferative disorder. The arrow indicates a Reed-Sternberg–like cell, and the arrowheads indicate Hodgkin-like cells. Original magnifications, ×1000 for spleen, ×400 for lymph node, and ×200 for liver, lung, kidney, and adrenal gland. *D*, Immunohistochemical staining for lymphocyte surface markers (CD3, CD20, CD23, and Mum1) and EBV-encoded proteins (latent membrane protein [LMP] 1 and Epstein-Barr nuclear antigen [EBNA] 2), as well as in situ hybridization for EBV-encoded small RNA (EBER), in a lymph node from a mouse with lymphoproliferative disorder. The bottom right panel represents double staining for EBER and CD20. Original magnifications, ×200 for all except EBER/CD20, which is ×400. *E* and *F*, Reverse-transcription polymerase chain reaction detection of latent-cycle *(E)* and lytic-cycle *(F)* EBV gene expression in tumors from EBV-infected hNOG mice. Spleen tumors from 3 different mice were examined for the expression of EBNA1, EBNA2, LMP1, LMP2A, LMP2B, EBER1, BZLF1, BMRF1, and BLLF1. RNA samples from a lymphoblastoid cell line (LCL) *(E)* and anti-IgG–treated Akata cells *(F)* were used as positive controls, and an RNA sample from EBV-negative Akata cells (*E* and *F*) was used as a negative control. Assays were done with (+) or without (−) reverse transcriptase (RT) in panel F. Expression of GAPDH was examined as a reference. *G*, Double staining of EBER and CD20 in the liver of an hNOG mouse that was persistently infected with EBV without developing lymphoproliferative disorder. EBER is stained navy in the nucleus, and CD20 is stained brown in the membrane. Original magnification, ×1000.

Table 2. Quantification of Epstein-Barr virus (EBV) DNA in persistently infected humanized NOG mice.

Organ	Mouse	
	N35-1[a]	N35-3[b]
Bone marrow	ND	4.1×10^4
Spleen	6.2×10^2	5.7×10^3
Liver	ND	2.7×10^4
Lymph node (neck)	1.6×10^3	6.9×10^3
Lymph node (axilla)	ND	2.6×10^2
Lymph node (mesentery)	ND	4.1×10^2
Lungs	2.7×10^3	1.0×10^4
Kidneys	1.2×10^3	4.8×10^4
Adrenal gland	4.4×10^1	8.0×10^5

NOTE. Data are the amounts of EBV DNA measured 22 weeks after infection, in copies per microgram of DNA. ND, not detectable.

[a] Infected at 1×10^{-1} TD_{50}.

[b] Infected at 1×10^1 TD_{50}.

Detection of antibodies specific to EBV. IgM antibody to the EBV BFRF3 protein was detected by immunoblotting essentially as described elsewhere [24], except that horseradish peroxidase–conjugated antibody specific to human IgM (Beckman Coulter) was used as secondary antibody. To prepare the glutathione *s*-transferase (GST)–BFRF3 fusion protein, a DNA fragment spanning the entire coding region of BFRF3 was amplified by PCR (sense primer, 5'-GGCTCGAATTCATGGCACGCCGGCTGCCC-3'; antisense primer, 5'-GGCTCGGATCCATACACCATGTTTCGTGCCC-3') and inserted to the GST fusion vector pSGENT2, to yield the plasmid pSGENT2-BFRF3. *Escherichia coli* cells harboring pSGENT2-BFRF3 were stimulated with isopropyl β-D-1-thiogalactopyranoside to induce the expression of GST-BFRF3, which was subsequently purified by use of the Bulk GST Purification Module (GE Healthcare).

RESULTS

EBV infection in hNOG mice. Transplantation of human $CD34^+$ HSCs in NOG mice and reconstitution of the human hematoimmune system were done as described elsewhere [18, 20]. In the initial attempts at infection, 1×10^3 TD_{50} of the Akata strain of EBV was inoculated into 6 hNOG mice, and EBV DNA was demonstrated in the peripheral blood of all of them (figure 1*A*). EBV DNA was first evident at 3–4 weeks after inoculation and reached peak levels of $\sim 1 \times 10^6$ EBV DNA copies/μg of DNA. All 6 mice became seriously ill between 5 and 10 weeks after inoculation, with signs of weight loss (figure 1*A*), general inactivity, and piloerection. In contrast, EBV DNA was not detected in the peripheral blood, bone marrow, thymus, spleen, lymph nodes, liver, kidneys, and lungs of 3 control NOG mice that were not transplanted with HSCs but were inoculated with the virus (data not shown). Similarly, no signs of EBV infection were observed in 3 control hNOG mice that were not inoculated with the virus (data not shown). In total, 43 NOG mice that had been humanized with HSCs from 9 different cord blood samples were inoculated with 1×10^3 TD_{50} of EBV, and in 38 of them the results were similar to those observed in the initial 6 mice, with high blood EBV load and severe deterioration in their general condition. Ten of them died and could not be examined further. The remaining 28 mice were killed, and signs of lymphoproliferative disorder were found at autopsy (see the below). These results demonstrate that hNOG mice can be infected with EBV, with a mostly fatal outcome at this virus dose.

EBV-induced lymphoproliferative disorder in hNOG mice. Autopsy of killed mice showed signs of lymphoproliferative disorder typically represented by an overt tumor in the spleen (figure 2*B*). In ~70% (20/28) of the mice autopsied, macroscopical signs of disseminated disease were found in the liver, lymph nodes, or kidneys (figure 2*A* and 2*B*). Seventeen mice were examined pathologically, and 15 of them showed typical histology of diffuse large B cell lymphoma, with remarkable similarity to the human lymphoproliferative disorder in the immunocompromised hosts (figure 2*C*). The tissues contained occasional immunoblasts, Reed-Sternberg–like cells, and Hodgkin-like cells (figure 2*C*). Marked infiltration of large transformed lymphoid cells was also demonstrated in liver, lymph nodes, kidneys, adrenal glands, and lungs (figure 2*C*). Real-time PCR detected high levels ($\sim 1 \times 10^5$ to $\sim 1 \times 10^6$ EBV DNA copies/μg of DNA) of EBV DNA in these organs, and the large transformed lymphoid cells were universally EBV positive by EBER ISH (figure 2*D*). Immunohistochemical analysis showed that the large transformed lymphoid cells were of the activated B cell phenotype, being reactive for CD20 and CD23 and not reactive for CD3 and CD10 (figure 2*D* and data not shown). They were also positive for Mum-1, a late- and postgerminal center cell marker. The EBER-positive cells were CD20-positive B cells (figure 2*D*), and no EBER-positive T cells were identified. Immunostaining revealed that most proliferating cells expressed EBNA2, whereas LMP1 was expressed in only a fraction of them (figure 2*D*). RT-PCR analysis of typical spleen tumors obtained from 3 different mice showed the expression of EBNA1, EBNA2, LMP1, LMP2A, LMP2B; and EBER, consistent with the latency III program of EBV gene expression (figure 2*E*). In addition, transcripts from lytic-cycle EBV genes, including BZLF1 (immediate-early), BMRF1 (early), and BLLF1 (late, encoding gp350/220), were identified (figure 2*F*).

Virus dose–dependent outcome of EBV infection in hNOG mice. To examine the influence of virus dose on the outcome of EBV infection, we inoculated serial dilutions of EBV preparation into 2 lots of hNOG mice, each consisting of 5 mice that had been humanized with the same HSC preparation. Consistent with the results described above, the 4 mice (2 from each lot) that received the higher doses (1×10^3 and 1×10^2 TD_{50}) of the

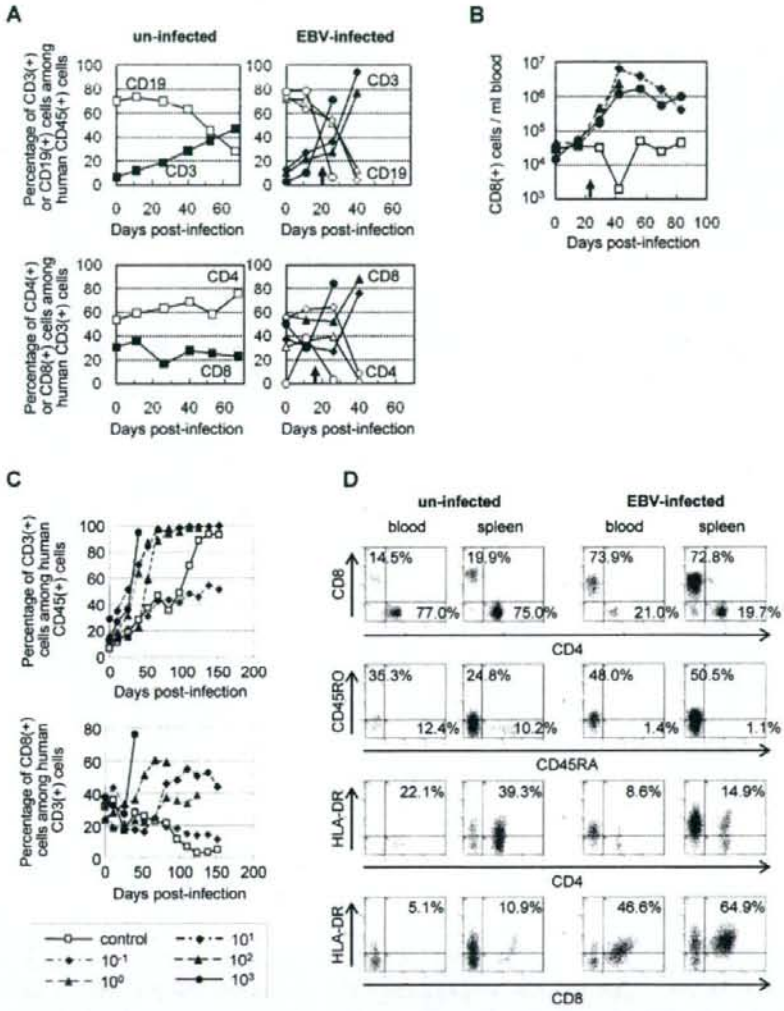

Figure 3. Surface marker expression by peripheral blood T cells in Epstein-Barr virus (EBV)–infected humanized NOG (hNOG) mice. *A*, Changes in the percentages of $CD3^+$ T cells and $CD19^+$ B cells among human $CD45^+$ leukocytes *(upper panels)* and in the percentages of $CD8^+$ cells and $CD4^+$ cells among $CD3^+$ cells *(lower panels)* after infection with EBV. Results obtained from 3 EBV-infected mice and an uninfected mice are shown. White symbols indicate the percentage of $CD19^+$ cells *(upper panels)* or $CD4^+$ cells *(lower panels)*; black symbols indicate the percentage of $CD3^+$ cells *(upper panels)* or $CD8^+$ cells *(lower panels)*. A vertical arrow in the graph area shows the time point at which EBV DNA was first detected in peripheral blood. *B*, Changes in the no. of $CD8^+$ T cells in the peripheral blood of EBV-infected hNOG mice. White symbols indicate uninfected mice, and black symbols indicate infected mice. Note that cell no. is plotted in a logarithmic scale. *C*, Viral dose–dependent T cell responses in hNOG mice inoculated with serially diluted EBV. Ten-fold serial dilutions of an EBV sample starting from 1×10^3 TD_{50} per inoculate were injected intravenously into NOG mice that had undergone transplantation with the same lot of human hematopoietic stem cells (HSCs). Changes in the percentages of $CD3^+$ T cells among human $CD45^+$ leukocytes *(upper panel)* and in the percentages of $CD8^+$ cells among $CD3^+$ cells *(lower panel)* after inoculation with EBV are shown. The viral dose for each mouse is shown in the key. *D*, Comparison of surface marker expression between EBV-infected mice and control mice. Two mice that underwent transplantation with the same lot of human HSCs were either inoculated with EBV or left uninfected; 10 weeks after inoculation, mononuclear cells obtained from peripheral blood or spleen were gated for the expression of human CD3 and then examined for the expression of CD8 and CD4 *(top panels)*, CD45RO and CD45RA *(second from top)*, HLA-DR and CD4 *(second from bottom)*, and HLA-DR and CD8 *(bottom)*.

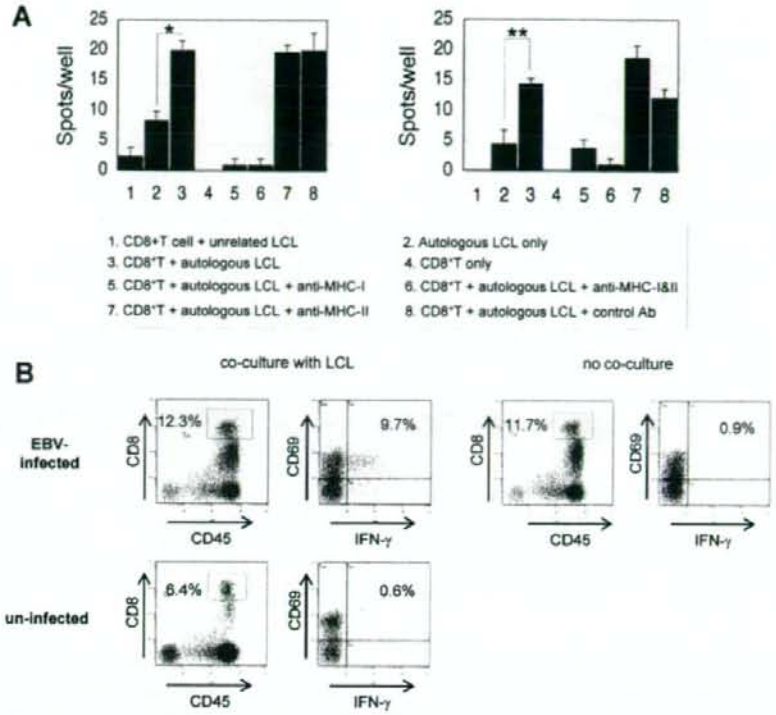

Figure 4. Epstein-Barr virus (EBV)–specific T cell response in humanized NOG (hNOG) mice. *A*, Enzyme-linked immunospot assay for the detection of human T cells producing interferon (IFN)–γ after stimulation with an EBV-positive lymphoblastoid cell line (LCL). $CD8^+$ cells isolated from EBV-infected hNOG mice were cocultured with an autologous LCL, and IFN-γ–secreting cells were counted (3, 5, 6, 7, and 8). To analyze restriction by major histocompatibility complex (MHC), antibody to HLA class I (anti–human HLA-ABC clone W6/32; eBioscience) (5), antibodies to both HLA class I and class II (6), antibody to HLA class II (anti–human HLA-DP,DQ,DR clone CR3/43; Dako) (7), or isotype-matched control antibody (8) were added to the culture. Control experiments included coculture of $CD8^+$ cells with an MHC-mismatched LCL (1), culture of the autologous LCL only (2), and culture of $CD8^+$ cells only (4). Results from 2 infected mice are shown. Five hundred $CD8^+$ cells per well were cultured in the experiment shown on the left, and 250 $CD8^+$ cells per well were cultured in that shown on the right. Spots were counted in triplicate in each of the 8 experimental groups, and the bars represent mean values and SEs. The unpaired Student's *t* test was used for statistical analysis. $^*P < .01$ and $^{**}P < .02$. *B*, Detection of human $CD8^+$ cells that produce IFN-γ in response to stimulation with an EBV-positive LCL by flow cytometry. $CD8^+$ cells were isolated from the spleen of an EBV-infected mouse and cocultured with the autologous LCL. Intracellular IFN-γ was stained and analyzed as described in Methods.

virus died of lymphoproliferative disorder ~5–10 weeks after inoculation. The remaining mice in both of the lots that received lower doses (1×10^1, 1×10^0, and 1×10^{-1} TD_{50}) survived acute infection and appeared normal throughout the observation period of 22 weeks. Although EBV DNA was detected at variable levels in their peripheral blood several weeks after inoculation, it returned to undetectable levels thereafter (figure 1*B*), suggesting that a certain protection mechanism worked to control EBV infection. Importantly, EBV DNA could be still detected in various organs, including spleen, liver, lungs, kidneys, and adrenal glands, at the end of the observation period (22 weeks), indicating that EBV persisted in these mice (table 2). Double staining for EBER and CD20 showed that EBV persisted in B cells (figure 2*G*). Macroscopical examination by autopsy at the end of the observation period did not reveal abnormality in these mice, except for moderate splenomegaly found in a mouse that received 1×10^1 TD_{50}. These results indicate that the outcome of EBV infection in hNOG mice varies with the virus dose; high doses of virus tend to cause fatal lymphoproliferative disorder, whereas lower doses induce apparently asymptomatic persistent infection.

EBV-specific T cell response in hNOG mice. Flow cytometry analysis demonstrated a dramatic increase in the percentage of $CD3^+$ T cells among the human $CD45^+$ leukocytes after infection with EBV. This increase in T cells was accompanied by an increase in the percentage of $CD8^+$ cells among human $CD3^+$ T cells. These changes were seen in virtually all infected mice, and the results from 3 mice are shown in figure 3*A*. The slow increase in the percentage of $CD3^+$ cells in the uninfected mouse represents the process of humanization (i.e., the development of hu-

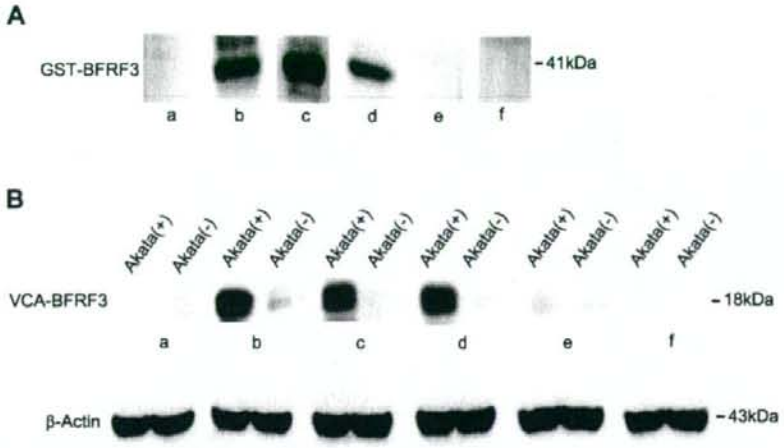

Figure 5. Demonstration of IgM antibody to the Epstein-Barr virus (EBV) BFRF3 protein in the serum of humanized NOG (hNOG) mice. *A*, Immunoblot with the glutathione *s*-transferase (GST)–BFRF3 fusion protein. Purified GST-BFRF3 fusion protein was examined with serum from an EBV-uninfected person *(a)*, an EBV-infected person *(b)*, EBV-infected hNOG mice (*c* and *d*), and an uninfected hNOG mice (*e* and *f*). *B*, Immunoblot with the lysate of EBV-producing Akata cells. Lysate of anti-IgG–treated Akata cells, labeled Akata(+), and of EBV-negative Akata cells, labeled Akata(−), was examined using serum from an EBV-uninfected person *(a)*, an EBV-infected person *(b)*, EBV-infected hNOG mice (*c* and *d*), and uninfected hNOG mice (*e* and *f*).

man T cells). This increase in $CD8^+$ cells were even more conspicuous when their definite number was counted (figure 3*B*). When hNOG mice were inoculated with serially diluted virus samples, a striking dose response was evident; mice inoculated with higher doses exhibited a more profound increase in $CD8^+$ cells at earlier time points (figure 3*C*). Further flow cytometry analyses showed that $CD45RO^+$ memory T cells, compared with $CD45RA^+$ T cells, increased in infected hNOG mice (figure 3*D*). Expression of a T cell activation marker, HLA-DR, was observed mainly in $CD8^+$ cells rather than in $CD4^+$ cells (figure 3*D*).

To demonstrate that these $CD8^+$ T cells were directed against EBV-infected cells, we examined IFN-γ secretion after stimulation with EBV-transformed cells. For this purpose, we first established an LCL using B cells isolated from the same cord blood that was used to isolate HSCs for transplantation. $CD8^+$ T cells, isolated from the peripheral blood of EBV-infected hNOG mice, were incubated with this autologous LCL, and cells secreting IFN-γ were detected by ELISPOT assay. For all 3 EBV-infected hNOG mice (which had been infected at 1×10^3 TD_{50}) thus examined, a significant number of spots were recognized in the wells in which $CD8^+$ T cells were mixed with the autologous LCL, whereas those cells incubated with unrelated LCL had many fewer spots (data from 2 mice are shown in figure 4*A*). $CD8^+$ T cells isolated from uninfected hNOG mice did not give a significant number of spots (data not shown). Release of IFN-γ was blocked by antibody specific to human major histocompatibility complex (MHC) class I but not by that specific to human MHC class II (figure 4*A*). These results clearly show that a T cell response restricted by human MHC class I was mounted against EBV-infected cells. In addition, in 5 of the 6 EBV-infected hNOG mice examined (infected at 1×10^3 TD_{50}), flow cytometry also demonstrated production of IFN-γ by $CD8^+$ T cells isolated from the spleen and stimulated with an autologous LCL (figure 4*B*).

EBV-specific antibody response in hNOG mice. Serum samples from 30 EBV-infected hNOG mice were examined by Western blotting for IgM antibodies reactive with a bacterially expressed GST-BFRF3 fusion protein. The BFRF3 protein is a major component of the virus capsid antigen of EBV [26]. The results are shown in figure 5*A* and indicated that four serum samples (from mice infected at 1×10^1 or 1×10^3 TD_{50}) contained IgM antibody reactive with it. These serum samples reacted also with the 18-kDa BFRF3-encoded protein in the lysate of Akata cells stimulated with IgG antibody to activate virus production (figure 5*B*). Similar experiments with human IgG–specific secondary antibody did not show a positive reaction with either GST-BFRF or $p18^{BFRF3}$. Six serum samples collected from uninfected hNOG mice reacted with neither the 18-kDa protein nor GST-BFRF3 (figure 5 and data not shown). These results indicate that hNOG mice have the ability to mount an IgM response to EBV.

DISCUSSION

The lymphoproliferative disease induced in hNOG mice is remarkably similar to the human lymphoproliferative disorder seen in immunocompromised hosts [27] with respect to histology, surface phenotype, and the type of EBV gene expression

(latency III). Reproduction of latency III in the present study makes for an interesting contrast with the previous model using NOD/*scid* mice, which exhibited the latency II pattern [10].

EBV infection in lower doses resulted in a transient increase in EBV DNA load in the peripheral blood, followed by apparently asymptomatic infection that persisted for at least 22 weeks. This type of asymptomatic EBV infection has not been described in nonprimate models of EBV infection and may be regarded as a model of human EBV latency. To compare this condition in NOG mice with EBV latency in humans precisely, we need to further investigate the nature of host cells (i.e., whether they are memory B cells), the pattern of EBV gene expression in them, and the involvement of anti-EBV immune responses in its maintenance.

In hNOG mice, human T cells develop in thymus tissue, in which epithelial cells are of murine origin [16]. It is therefore interesting that they could mount a T cell response restricted by human MHC class I. Although this suggests that positive selection of human T cells occurred in hNOG mice, the mechanism of T cell education remains unclear. Alloantigen-specific and human MHC class I–restricted T cell cytotoxicity has been reported in hNOG mice [15, 16]. An EBV-induced T cell response was evident in mice that received high doses of virus and developed lymphoproliferative disorder, suggesting that the T cell response in hNOG mice was not sufficient to control EBV-induced lymphoproliferation when they were infected at high doses. That only a minor fraction of $CD8^+$ T cells appeared to be EBV specific, as evidenced by ELISPOT assay and flow cytometry, may explain this result, at least partially. A humoral immune response to EBV has not been documented in previous mouse models of EBV infection, and therefore the NOG mouse may provide a valuable tool to analyze the mechanism and the protective roles of antibody response in EBV infection. We have to date clearly identified only IgM antibody to the 18-kDa component of virus capsid antigen in a minor fraction (4/30) of infected mice. We are currently attempting to improve sensitivity and to see whether hNOG mice can mount a more efficient and divergent antibody response to the virus, possibly including the production of IgG antibodies. Because both the T cell–mediated and the humoral immune response are elicited in hNOG mice, they may be useful in the evaluation of candidate EBV vaccines.

Very recently, humanized mice based on other immunodeficient mouse strains were prepared, and EBV was used as a typical pathogen to analyze their immune functions. Traggiai et al. [12] infected humanized $Rag2^{-/-}IL\text{-}2R\gamma^{-/-}$ mice with EBV and documented an in vitro proliferative response by $CD8^+$ T cells to an autologous LCL. Melkus et al. [11], on the other hand, humanized NOD/*scid* mice by transplanting human fetal liver, thymus, and HSCs and succeeded in inducing an EBV-specific T cell immune response as well as an innate immune response to toxic shock syndrome toxin 1. These 2 studies were performed mainly using immunological standpoints and did not provide detailed data from virological investigations. An advantage of the NOG mouse model described here is that it does not require a fine surgical procedure using human fetal tissue; therefore, NOG mice can be easily provided in large quantities.

In immunocompromised humans, failure of immunosurveillance may lead to the development of lymphoproliferative disorder. We expect that the NOG mouse model can be used to analyze the exact relationship between immunodeficiency and the development of lymphoproliferative disorder. Immune responses in the hNOG mouse can be modulated by immunosuppressive drugs (such as cyclosporine A) or HIV, and the development of lymphoproliferative disorder can be analyzed with special reference to the nature and level of immunodeficiency. This kind of study, which has not been possible with conventional *scid* mice, may reveal an exact condition in which lymphoproliferative disorder develops and may thereby aid the development of a specified immunosuppressive procedure that evades this condition and precludes the risk of lymphoproliferative disorder.

In summary, the NOG mouse is able to recapitulate various essential elements of human EBV infection and is therefore, to our knowledge, the most comprehensive small-animal model of EBV infection described to date. It should be a valuable tool for the study of the pathogenesis, prevention, and treatment of EBV infection.

Acknowledgments

We thank Satoshi Itakura, Fuyuko Kawano, Eri Yamada, Miki Mizukami, and Ken Watanabe for technical assistance. We thank Shizuko Minegishi for advice on flow cytometry, Atsushi Komano for advise on the enzyme-linked immunospot assay, Ayako Demachi-Okamura and Kiyotaka Kuzushima for advice on detection of Epstein-Barr virus–specific T cells, and Shosuke Imai for helpful discussions. We thank the Tokyo Cord Blood Bank for supplying cord blood.

References

1. Rickinson AB, Kieff E. Epstein-Barr virus. In: Knipe DM, Howley PM, eds. Fields virology. Philadelphia: Lippincott Williams & Wilkins, **2001**: 2575–628.
2. Kieff E, Rickinson AB. Epstein-Barr virus and its replication. In: Knipe DM, Howley PM, eds. Fields virology. 4th ed. Philadelphia: Lippincot Williams & Wilkins, **2001**:2511–74.
3. Young LS, Finerty S, Brooks L, Scullion F, Rickinson AB, Morgan AJ. Epstein-Barr virus gene expression in malignant lymphomas induced by experimental virus infection of cottontop tamarins. J Virol **1989**; 63: 1967–74.
4. Miller G, Shope T, Coope D, et al. Lymphoma in cotton-top marmosets after inoculation with Epstein-Barr virus: tumor incidence, histologic spectrum antibody responses, demonstration of viral DNA, and characterization of viruses. J Exp Med **1977**; 145:948–67.
5. Cho Y, Ramer J, Rivailler P, et al. An Epstein-Barr-related herpesvirus from marmoset lymphomas. Proc Natl Acad Sci USA **2001**; 98:1224–9.
6. Moghaddam A, Rosenzweig M, Lee-Parritz D, Annis B, Johnson RP, Wang F. An animal model for acute and persistent Epstein-Barr virus infection. Science **1997**; 276:2030–3.
7. Mosier DE, Gulizia RJ, Baird SM, Wilson DB. Transfer of a functional human immune system to mice with severe combined immunodeficiency. Nature **1988**; 335:256–9.

8. Okano M, Taguchi Y, Nakamine H, et al. Characterization of Epstein-Barr virus-induced lymphoproliferation derived from human peripheral blood mononuclear cells transferred to severe combined immunodeficient mice. Am J Pathol **1990**; 137:517–22.
9. Rowe M, Young LS, Crocker J, Stokes H, Henderson S, Rickinson AB. Epstein-Barr virus (EBV)-associated lymphoproliferative disease in the SCID mouse model: implications for the pathogenesis of EBV-positive lymphomas in man. J Exp Med **1991**; 173:147–58.
10. Islas-Ohlmayer M, Padgett-Thomas A, Domiati-Saad R, et al. Experimental infection of NOD/SCID mice reconstituted with human CD34+ cells with Epstein-Barr virus. J Virol **2004**; 78:13891–900.
11. Melkus MW, Estes JD, Padgett-Thomas A, et al. Humanized mice mount specific adaptive and innate immune responses to EBV and TSST-1. Nat Med **2006**; 12:1316–22.
12. Traggiai E, Chicha L, Mazzucchelli L, et al. Development of a human adaptive immune system in cord blood cell-transplanted mice. Science **2004**; 304:104–7.
13. Hiramatsu H, Nishikomori R, Heike T, et al. Complete reconstitution of human lymphocytes from cord blood CD34+ cells using the NOD/SCID/γ_c^{null} mice model. Blood **2003**; 102:873–80.
14. Ito M, Hiramatsu H, Kobayashi K, et al. NOD/SCID/γ_c^{null} mouse: an excellent recipient mouse model for engraftment of human cells. Blood **2002**; 100:3175–82.
15. Yahata T, Ando K, Nakamura Y, et al. Functional human T lymphocyte development from cord blood CD34+ cells in nonobese diabetic/Shi-scid, IL-2 receptor gamma null mice. J Immunol **2002**; 169:204–9.
16. Ishikawa F, Yasukawa M, Lyons B, et al. Development of functional human blood and immune systems in NOD/SCID/IL2 receptor γ chain^{null} mice. Blood **2005**; 106:1565–73.
17. Miyazato P, Yasunaga J, Taniguchi Y, Koyanagi Y, Mitsuya H, Matsuoka M. De novo human T-cell leukemia virus type 1 infection of human lymphocytes in NOD-SCID, common gamma-chain knockout mice. J Virol **2006**; 80:10683–91.
18. Watanabe S, Terashima K, Ohta S, et al. Hematopoietic stem cell-engrafted NOD/SCID/IL2Rgamma null mice develop human lymphoid systems and induce long-lasting HIV-1 infection with specific humoral immune responses. Blood **2007**; 109:212–8.
19. Dewan MZ, Terashima K, Taruishi M, et al. Rapid tumor formation of human T-cell leukemia virus type 1-infected cell lines in novel NOD-SCID/gammac^{null} mice: suppression by an inhibitor against NF-kappaB. J Virol **2003**; 77:5286–94.
20. Watanabe S, Ohta S, Yajima M, et al. Humanized NOD/SCID/IL2Rγ^{null} mice transplanted with hematopoietic stem cells under nonmyeloablative conditions show prolonged life spans and allow detailed analysis of human immunodeficiency virus type 1 pathogenesis. J Virol **2007**; 81: 13259–64.
21. Takada K, Ono Y. Synchronous and sequential activation of latently infected Epstein-Barr virus genomes. J Virol **1989**; 63:445–9.
22. Condit RC. Principles of virology. In: Knipe DM, Howley PM, eds. Fields virology. Philadelphia: Lippincott Williams & Wilkins, **2001**:19–51.
23. Kimura H, Morita M, Yabuta Y, et al. Quantitative analysis of Epstein-Barr virus load by using a real-time PCR assay. J Clin Microbiol **1999**; 37:132–6.
24. Nakamura H, Iwakiri D, Ono Y, Fujiwara S. Epstein-Barr-virus-infected human T-cell line with a unique pattern of viral-gene expression. Int J Cancer **1998**; 76:587–94.
25. Kuzushima K, Hoshino Y, Fujii K, et al. Rapid determination of Epstein-Barr virus-specific $CD8^+$ T-cell frequencies by flow cytometry. Blood **1999**; 94:3094–100.
26. van Grunsven WM, Nabbe A, Middeldorp JM. Identification and molecular characterization of two diagnostically relevant marker proteins of the Epstein-Barr virus capsid antigen complex. J Med Virol **1993**; 40: 161–9.
27. Rezk SA, Weiss LM. Epstein-Barr virus-associated lymphoproliferative disorders. Hum Pathol **2007**; 38:1293–304.

Modulation of TNF-α-converting enzyme by the spike protein of SARS-CoV and ACE2 induces TNF-α production and facilitates viral entry

Shiori Haga*†, Norio Yamamoto‡, Chikako Nakai-Murakami*†, Yoshiaki Osawa*†§, Kenzo Tokunaga¶, Tetsutaro Sata¶, Naoki Yamamoto‖, Takehiko Sasazuki†, and Yukihito Ishizaka*†**

*Department of Intractable Diseases, †International Medical Center of Japan, 162-8655 Tokyo, Japan; ‡Department of Molecular Virology, Graduate School, Tokyo Medical and Dental University, 101-0062 Tokyo, Japan; and ¶Department of Pathology and ‖AIDS Research Center, National Institute of Infectious Diseases, 162-8640 Tokyo, Japan

Edited by Diane E. Griffin, Johns Hopkins Bloomberg School of Public Health, Baltimore, MD, and approved March 6, 2008 (received for review November 28, 2007)

Severe acute respiratory syndrome coronavirus (SARS-CoV) is a high-risk infectious pathogen. In the proposed model of respiratory failure, SARS-CoV down-regulates its receptor, angiotensin-converting enzyme 2 (ACE2), but the mechanism involved is unknown. We found that the spike protein of SARS-CoV (SARS-S) induced TNF-α-converting enzyme (TACE)-dependent shedding of the ACE2 ectodomain. The modulation of TACE activity by SARS-S depended on the cytoplasmic domain of ACE2, because deletion mutants of ACE2 lacking the carboxyl-terminal region did not induce ACE2 shedding or TNF-α production. In contrast, the spike protein of HNL63-CoV (NL63-S), a CoV that uses ACE2 as a receptor and mainly induces the common cold, caused neither of these cellular responses. Intriguingly, viral infection, judged by real-time RT-PCR analysis of SARS-CoV mRNA expression, was significantly attenuated by deletion of the cytoplasmic tail of ACE2 or knock-down of TACE expression by siRNA. These data suggest that cellular signals triggered by the interaction of SARS-CoV with ACE2 are positively involved in viral entry but lead to tissue damage. These findings may lead to the development of anti-SARS-CoV agents.

shedding | cytoplasmic tail | HNL63-CoV | TNF-α

Severe acute respiratory syndrome coronavirus (SARS-CoV) is an infectious pathogen known to have caused acute respiratory distress in >8,000 patients with a mortality rate of ≈10% (1). Although outbreaks of SARS-CoV are now well controlled, the mechanism of severe respiratory failure in infected patients is unknown. Angiotensin-converting enzyme 2 (ACE2), an ACE homolog that functions as a positive regulator of the renin-angiotensin system (RAS) (2, 3), was identified as a receptor of SARS-CoV (4). A possible indicator of a severe clinical outcome, the spike protein of SARS-CoV (SARS-S) was found to down-regulate ACE2 expression (5). ACE2 knockout (KO) mice were also shown to be susceptible to severe respiratory failure after chemical challenge (5, 6), and ACE2 has been shown to moderate ACE-induced intracellular inflammation, suggesting that the mechanism of ACE2 down-regulation may explain the molecular basis of SARS-CoV-related severe respiratory distress.

HNL63-CoV, a CoV (7) that causes the common cold, was recently found to use ACE2 for viral infection (8), and it was further shown that the spike protein of HNL63-CoV (NL63-S) binds ACE2 directly (9). NL63-S and SARS-S show 21% identity (10), whereas that between NL63-S and the spike protein of HCoV-229E, which uses CD13 [a completely different carboxy (C)-peptidase] as a cellular receptor (11), is 55%. It is important to note that, despite their phylogenetically distinct properties and their producing different clinical outcomes, SARS-CoV and HNL63-CoV both use ACE2.

Based on these observations, we hypothesized that the functional modulation of ACE2 may be differentially induced by SARS-S and NL63-S. To test this prediction, we first clarified the mechanism of SARS-S-induced ACE2 down-regulation, and then compared the cellular responses induced by each protein. We found that SARS-S induced TNF-α-converting enzyme (TACE)-dependent shedding of the ectodomain of ACE2, and that the process was coupled with TNF-α production (12). Experiments using deletion mutants of ACE2 revealed that the cytoplasmic tail of ACE2 is required for shedding. Furthermore, viral infection with SARS-CoV was significantly decreased in cells expressing mutant versions of ACE2 lacking the cytoplasmic domain. In addition, siRNAs of *TACE* and *ACE2* blocked viral infection. These observations suggest that TACE activity is modulated by SARS-CoV via the cytoplasmic domain of ACE2, and that it facilitates viral entry but also causes tissue damage through TNF-α production. Together with data showing that NL63-S does not evoke these cellular responses, our results indicate that the cellular components involved in SARS-S-induced ACE2 shedding are good targets for anti-SARS-CoV therapeutics.

Results

SARS-S Induces Shedding of the Ectodomain of ACE2. We first examined the mechanism of ACE2 down-regulation after SARS-S binding. In total cellular extracts prepared from Vero E6 cells infected with a pseudotyped virus expressing S protein (S-virus), ACE2 expression was reduced, whereas the expression of an 80-kDa protein in the supernatants was increased (Fig. 1*a*, lanes 4 and 5). Interestingly, this 80-kDa peptide was not detected by an antibody raised against the cytoplasmic domain of ACE2 (Fig. 1*a*, lanes 4 and 5, middle row in *Lower*). Conversely, a control pseudotyped lentivirus expressing vesicular stomatitis virus G protein (VSV-G) did not induce any change in ACE2 expression (Fig. 1*a*, lanes 6–10). Moreover, recombinant SARS-S showed the same effects (Fig. 1*b*, lanes 4–6, arrows), whereas binding-defective mutants of the protein (Fig. 1*c*, ΔC and ΔN) did not (Fig. 1*d*, lanes 2–4). Consistent with a report showing that the secreted form of ACE2 is the active form (shed form) (2), C-peptidase activity was detected in the supernatants of cultured cells treated with SARS-S

Author contributions: T. Sasazuki and Y.I. designed research; S.H., Norio Yamamoto, C.N.-M., Y.O., and Y.I. performed research; K.T., T. Sata, Naoki Yamamoto, and Y.I. contributed new reagents/analytic tools; S.H. and Y.I. analyzed data; and S.H. and Y.I. wrote the paper.

The authors declare no conflict of interest.

This article is a PNAS Direct Submission.

§Present address: Department of molecular bioscience, Faculty of Pharmaceutical Sciences, Health Sciences University of Hokkaido, 1757 Kanazawa, Tobetsu-cho, Ishikari-gun, Hokkaido 061-0293, Japan.

**To whom correspondence should be addressed. E-mail: zakay@ri.imcj.go.jp.

This article contains supporting information online at www.pnas.org/cgi/content/full/0711241105/DCSupplemental.

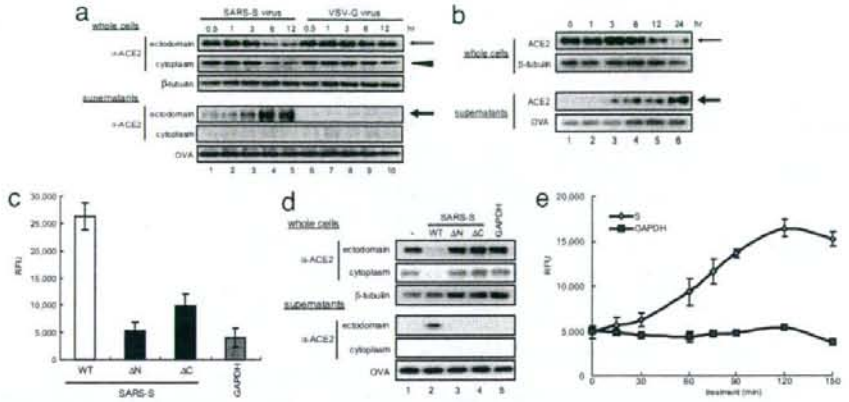

Fig. 1. Induction of ACE2 shedding by the specific binding of SARS-S and ACE2. (*a*) ACE2 shedding is induced by SARS-S. After infection with SARS-S, total extracts (*Upper*) or the supernatants (*Lower*) of cultured Vero E6 cells were analyzed. The thin arrow and arrowhead indicate the 120-kDa ACE2 protein detected by antibodies against the ectodomain and cytoplasmic domain, respectively. The bold arrow indicates the 80-kDa ACE2 detected by an antibody against the ACE2 cytoplasmic domain (lanes 2–5), which was not generated by control VSV-G virus (lanes 6–10). The proteins present in the culture supernatants were recovered with OVA by TCA precipitation. β-Tubulin was used as a loading control. (*b*) Recombinant SARS-S induces ACE2 shedding. Cells were treated with 100 μg/ml SARS-S (residues 284–541), and ACE2 in the culture supernatant was examined as described in *a*. (*c*) Binding of the SARS-S mutants to ACE2. Two SARS-S mutants, ΔN (residues 332–541) and ΔC (residues 284–490), were prepared according to a report showing the minimum region of SARS-S required for ACE2 binding (27), and their binding activities to ACE2 were examined (see also *Materials and Methods*). (*d*) Specific binding to ACE2 is required for ACE2 shedding. After treatment with the ΔN and ΔC SARS-Ss, the amount of ACE2 in the culture supernatant was examined as described in *a*. (*e*) C-peptidase activity of the shed ACE2. The C-peptidase activity in the culture supernatant of SARS-S-treated Vero E6 cells was measured (filled diamonds) (see *Materials and Methods*). GAPDH was used as a negative control (filled squares).

(Fig. 1*e*). Therefore, we concluded that SARS-S down-regulates ACE2 by inducing shedding of the ACE2 ectodomain.

TACE Is a Critical Cellular Factor in SARS-S-Induced ACE2 Shedding. It has been shown that TACE and ADAM17, a member of the ADAM (a disintegrin and metalloprotease) family (12, 13), are required for the induction of ACE2 shedding by phorbol esters [phorbol-12-myristate-13-acetate (PMA)] (14). Therefore, we examined the effects of TAPI-0, an inhibitor of TACE (15), on SARS-S-induced ACE2 shedding. As shown in Fig. 2*a*, TAPI-0 efficiently attenuated C-peptidase activity in the culture supernatant. Western blot analysis also indicated that TAPI-0 inhibited SARS-S-induced ACE2 shedding (Fig. 2*b*, lanes 5 and 6). To further determine the involvement of TACE, ACE2 shedding was examined by forced expression of *TACE* cDNA in transformed mouse fibroblasts derived from *tace*-KO mouse fibroblasts (*tace*-KO cells) (16). As shown in Fig. 2*c*, the *tace*-KO cells exhibited SARS-S-induced ACE2 shedding when both *TACE* and *ACE2* cDNA was introduced (Fig. 2*c*, lanes 4 and 5). To obtain direct evidence that TACE plays an important role in ACE2 shedding, *TACE* siRNA was introduced into Huh-7 cells and SARS-S-induced ACE2 shedding was examined. Huh-7 is a human hepatoma cell line permissive for SARS-CoV infection (17, 18). As shown in Fig. 2*d*, ACE2 shedding by SARS-S was significantly

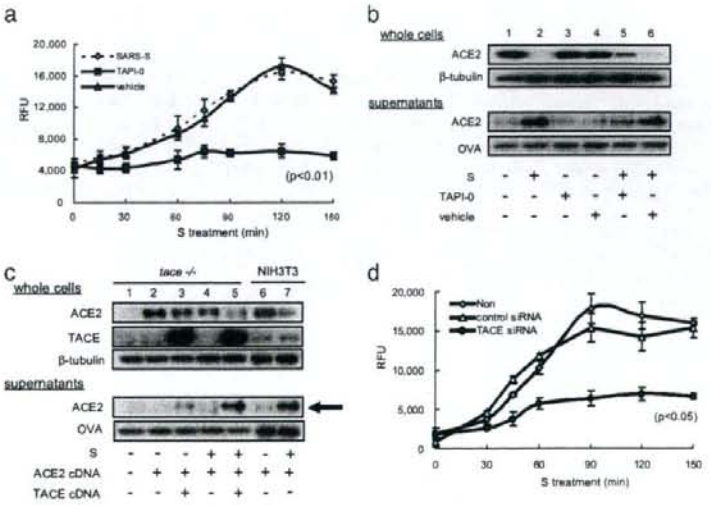

Fig. 2. ACE2 shedding depends on TACE. (*a*) Inhibitory effects of TAPI-0 on ACE2 shedding. Vero E6 cells were cultured with or without 100 nM TAPI-0, and the amounts of C-peptidase activity in the culture supernatants were measured. SARS-S was used at a concentration of 100 μg/ml. (*b*) TACE inhibitor blocked SARS-S-induced ACE2 shedding. The experiments described in *a* were carried out and ACE2 was detected by Western blot analysis. (*c*) ACE2 shedding depends on TACE activity. *tace*-KO cells were transfected with cDNAs encoding ACE2 or TACE and then treated with 100 μg/ml SARS-S for 6 h. Shed ACE2 was then detected (bold arrow). (*d*) The effects of *TACE* siRNA on ACE2 shedding. After the introduction of *TACE* or control siRNA, SARS-S-induced ACE2 shedding was examined by measuring the amount of C-peptidase activity in the culture supernatant. Huh-7 cells, a human cell line that expresses endogenous ACE2 and TACE (see Fig. 5*c*), were analyzed.

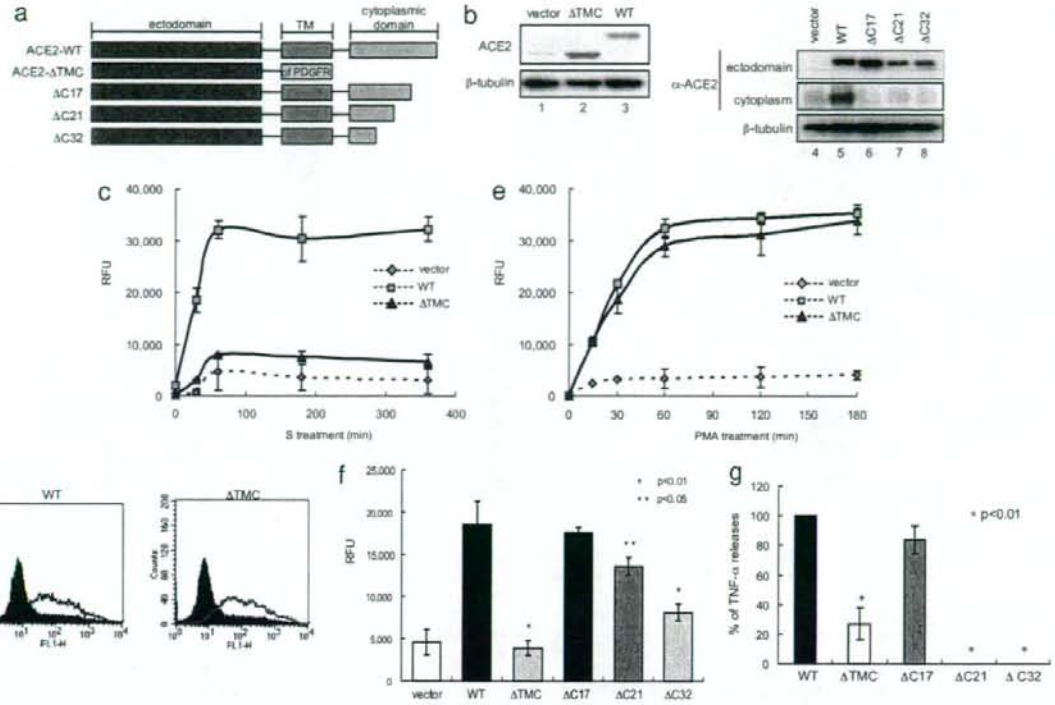

Fig. 3. ACE2 shedding by SARS-S requires the cytoplasmic domain of ACE2. (*a*) Schematic diagrams of the ACE2 cytoplasmic domain mutants. ΔTMC-ACE2 contains only the ectodomain of ACE2 with the transmembrane domain of PDGF receptor. (*b*) Expression of the ACE2 cytoplasmic domain mutants. The molecular weights of full-length ACE2 (lane 3) and all mutants except ΔTMC-ACE2 (lanes 6–8) were ≈120 kDa. The molecular weight of ΔTMC-ACE2 was ≈95 kDa (lane 2). (*c*) ΔTMC-ACE2 did not show ectodomain shedding with SARS-S. After treatment with SARS-S, the amounts of C-peptidase activity in the culture supernatant of cells expressing WT (filled squares) or ΔTMC-ACE2 (filled diamonds) were examined. (*d*) Binding of ΔTMC-ACE2 to SARS-S. Recombinant SARS-S was expressed and purified as a chimeric protein with the Fc portion of human IgG (Fc), and bound SARS-S was detected by FACS analysis, using FITC-labeled anti-human IgG (9). Each line indicates the cells that were positive for bound SARS-S. Solid peaks depict cells bound nonspecifically with control IgG-Fc. (*e*) ΔTMC-ACE2 was competent for ectodomain shedding by PMA. After treatment with PMA for 1 h, the amounts of C-peptidase activity in the culture supernatant of cells expressing WT (filled squares) or ΔTMC-ACE2 (filled diamonds) were examined. (*f*) The ectodomain shedding of ACE2 depends on the cytoplasmic domain. The levels of C-peptidase activity in the culture supernatant of cells expressing various ACE2 mutants were measured. (*g*) TACE activation requires the cytoplasmic domain of ACE2. TACE activation, judged by the production of TNF-α in the culture supernatant, was induced by both WT and ΔC17-ACE2. TNF-α was detected 20 h after SARS-S treatment.

attenuated by *TACE* siRNA. As shown in Fig. 5*c*, *TACE* siRNA successfully reduced endogenous TACE expression.

The ACE2 Cytoplasmic Domain Is Required for SARS-S-Induced ACE2 Shedding. Cellular TACE was activated by the interaction of SARS-S with ACE2, strongly suggesting the involvement of the cytoplasmic domain of ACE2 in this phenomenon. To confirm this suggestion, we prepared several mutants lacking the C-terminal region of ACE2 (Fig. 3*a*). After confirming the expression of each mutant protein (Fig. 3*b*), we examined shedding of the ectodomain by SARS-S. SARS-S-induced ACE2 shedding was not observed with a chimeric mutant in which the transmembrane and cytoplasmic domains of ACE2 were eliminated [transmembrane and cytoplasmic domains (ΔTMC) Fig. 3*c*]. This mutant was able to bind SARS-S (Fig. 3*d*), and it was susceptible to ectodomain shedding when the cells were stimulated with PMA (Fig. 3*e*). Experiments with additional deletion mutants revealed that the last 17 aa of the ACE2 C terminus were dispensable for ACE2 shedding (Fig. 3*f*). Similar to ACE2 shedding, the production of TNF-α was detected in the culture supernatants of cells expressing WT and ΔC17-ACE2 (Fig. 3*g*). In contrast, no TNF-α production was observed in cells expressing deletion mutants of the cytoplasmic tail of ACE2 (Fig. 3*g*, $P < 0.01$).

The ACE2 Cytoplasmic Domain and TACE Are Positively Involved in Virus Entry. We investigated the role of the cytoplasmic tail of ACE2 and TACE in viral infection. In a reporter assay based on a pseudotyped lentiviral system, no difference in infection was detected between cells expressing WT and ΔTMC-ACE2 (Fig. 4*a*). Although this observation is consistent with previous reports, we observed a reproducible difference in viral entry based on the intracellular p24 concentration after infection with the same virus (Fig. 4*b*). To obtain conclusive evidence, we infected the cells with SARS-CoV and quantified SARS-CoV mRNA by real-time RT-PCR. As shown in Fig. 4*c*, deletion of the cytoplasmic tail greatly reduced viral infection. The efficiency of infection was also markedly reduced in cells infected with ΔC21 or ΔC32-ACE2 (Fig. 4*d*), even with ΔC17-ACE2.

We next examined the role of TACE in viral infection, using *TACE* siRNA. As shown in Fig. 4*e*, viral entry was significantly attenuated ($P < 0.05$) by the siRNA, whereas control or *ADAM10* (control metalloprotease) siRNA did not decrease the incidence of viral infection. It is important to note that *ACE2* siRNA signifi-

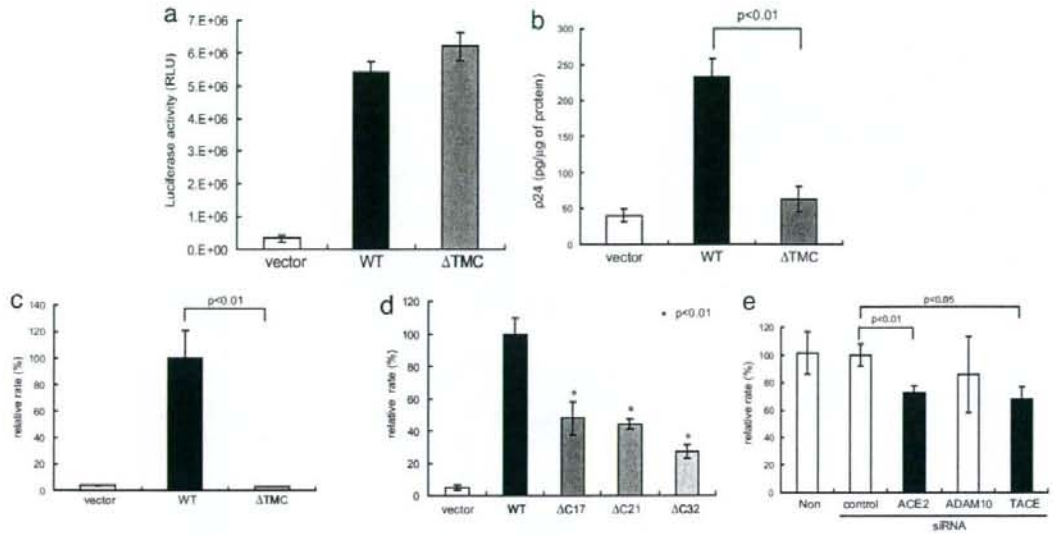

Fig. 4. The cytoplasmic tail of ACE2 and TACE promote infection by SARS-CoV. (*a*) No difference in infection efficiency was detected by reporter assay, using a pseudotyped lentivirus system. After infection of HEK293T cells expressing WT or ΔTMC-ACE2 with a pseudotyped lentivirus encoding luciferase, luciferase activity was measured. Luciferase activity was assayed in triplicate. (*b*) Detection of differences in viral infection efficiency based on the intracellular p24 level. The experiment in *a* was followed by measurement of the intracellular p24 level, using an ELISA kit. (*c*) A marked difference in viral infection efficiency detected by real-time RT-PCR. Each cell was harvested and analyzed 2 h after infection with SARS-CoV. The data were normalized by 18S ribosomal RNA. (*d*) The cytoplasmic tail is required for efficient viral infection. SARS-CoV was used to infect cells expressing deletion mutants of the cytoplasmic tail of ACE2 (Fig. 3*a*). Then, real-time RT-PCR was carried out as described in *c*. (*e*) TACE is required for efficient viral entry. The efficiency of viral entry into Huh-7 cells was examined before and after the introduction of *TACE* or *ACE2* siRNAs. *TACE* siRNA [but not *ADAM10* (metalloprotease control) siRNA] significantly attenuated viral entry ($P < 0.05$). *ACE2* siRNA also decreased viral infection ($P < 0.01$).

cantly decreased the SARS-CoV mRNA copy number (Fig. 4*e*, $P < 0.01$), indicating that infection by SARS-CoV via ACE2 was successfully detected by real-time RT-PCR. As shown in Fig. 5*c*, each siRNA efficiently blocked expression of the target protein. These observations indicate that the cytoplasmic tail of ACE2 and TACE are positively involved in SARS-S-dependent viral infection. In addition, the level of intracellular p24 after infection with pseudotyped lentivirus is a good indicator of viral entry.

HNL63-CoV Spike Protein Does Not Induce ACE2 Shedding or TACE Activation. To determine the specificity of the ACE2 shedding and TNF-α production induced by SARS-CoV, we investigated the functions of HNL63-CoV. In marked contrast to SARS-S, NL63-S did not induce ACE2 shedding (Fig. 5*a*, lane 4), although it was able to use ACE2 as a cellular receptor (Fig. 5*d*). Furthermore, NL63-S did not induce TNF-α production (Fig. 5*b*). To characterize the differential mode of infection between SARS-S and NL63-S, we examined the effects of siRNAs against *ACE2*, *TACE*, and *ADAM10*, and we examined viral entry by measuring the level of intracellular p24. We began by confirming that each siRNA or combination of siRNAs successfully interfered with expression of the endogenous gene products (Fig. 5*c*). As shown in Fig. 5*d*, the *ACE2* and *TACE* siRNAs efficiently blocked viral entry ($P < 0.05$ and 0.01, respectively), whereas the *ADAM10* siRNA did not. However, we detected no definite effect of *TACE* siRNA on NL63-S infection. The *ACE2* and *TACE* or *ADAM10* siRNAs, however, did significantly inhibit NL63-S viral entry.

Taken together, these observations suggest that ACE2 and TACE are differently required for infection by SARS-S and NL63-S and that the functional role of TACE is more prominent for SARS-S than for NL63-S.

Discussion

Down-regulation of ACE2 was proposed to be associated with a severe clinical outcome in cases of SARS-CoV infection, but the mechanism remained to be clarified. In the present study, we found that SARS-S induces ACE2 shedding via a process that is tightly coupled with TNF-α production. In contrast, the spike protein of HNL63-CoV, a CoV and etiological pathogen of the common cold that uses ACE2 as its cellular receptor, did not induce such cellular responses. These observations suggest that ACE2 shedding and its causative cellular signals are attributable to SARS-CoV-induced tissue damage.

As shown in Fig. 3*g*, the induction of TNF-α production by SARS-S depends on the cytoplasmic tail of ACE2 and TACE activity. Because treatment with SARS-S did not increase the expression of the membrane-bound precursor of TNF-α [supporting information (SI) Fig. S1], it seems that TACE activity is directly affected by the attachment of SARS-S to ACE2. Lambert *et al.* (14) proposed that PMA-driven ACE2 shedding solely depended on TACE. In addition, the results of our experiments using siRNAs against *TACE* and *ADAM10* revealed that SARS-S-induced ACE2 shedding depends on TACE activity. Interestingly, however, the forced expression of ADAM9 or 10 rendered *tace*-KO cells competent for SARS-S-dependent viral infection (Fig. S2), implying that TACE may be complemented by the overexpression of other ADAMs. We also observed that rottlerin, a PKC inhibitor (19), partially blocked the phenomenon (Fig. S3). It is likely that functional modulation of the cytoplasmic tail of ACE2 triggers multiple cellular signals involving PKC activation.

Intriguingly, we found that the entry of SARS-CoV depends on the cytoplasmic tail of ACE2 and TACE activity, which was inconsistent with previous reports indicating that the cytoplasmic tail of ACE2 is dispensable for viral infection (18, 20). However,

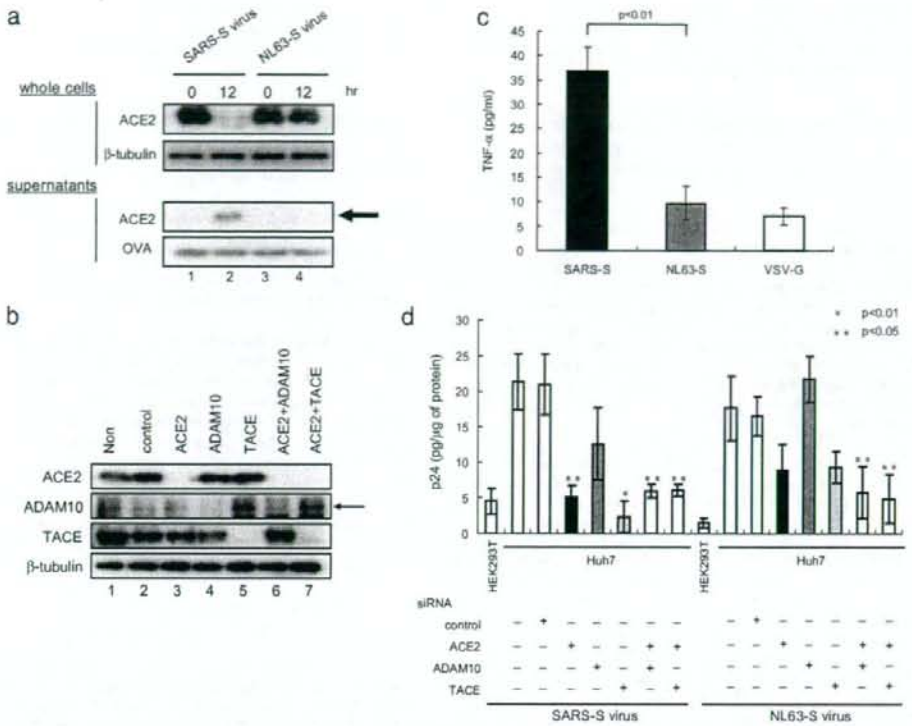

Fig. 5. NL63-S does not induce ACE2 shedding. (*a*) No ACE2 shedding was observed when using NL-63-S. After infection of Vero E6 cells with NL63-S or SARS-S, ACE2 was examined as described in Fig. 1a. (*b*) NL63-S does not induce TNF-α production. TNF-α was measured in the culture supernatants of ACE2-expressing HEK293T cells. The supernatants were collected 12 h after infection with NL63-S or SARS-S. (*c*) Effects of siRNAs on the expression of endogenous gene products. Huh-7 cells were transduced with siRNAs against *TACE*, *ACE2*, and *ADAM10*, and the expression of each protein was examined. Lanes 3, 4, and 5 indicate the endogenous expression of ACE2, ADAM10, and TACE, respectively. Lanes 6 and 7 depict the effects of the combined use of siRNAs on protein expression. (*d*) The differential requirements of TACE for viral entry by NL63-S and SARS-S. Huh-7 cells were infected with SARS-S and NL63-S viruses for 4 h, and the efficiency of viral entry was examined by measuring the intracellular p24 level. Note that the entry of SARS-S was reduced by siRNAs against *ACE2* and *TACE*, whereas NL63-S was not.

these previous studies were performed by using pseudotyped lentiviruses. As shown in Fig. 4*a*, we also detected no differences in reporter gene expression in cells expressing WT-ACE2 and ΔTMC-ACE2. However, viral entry, as judged by the amount of p24, a component of the HIV-1-based lentivirus (Fig. 4*b*), was significantly higher in cells expressing WT-ACE2 than in those expressing ΔTMC-ACE2. Because the replication of SARS-CoV does not require viral integration into the host genome, we assumed that a reporter assay based on a pseudotyped lentivirus was not relevant for evaluating the roles of the factors involved in SARS-CoV infection. Given these expectations, we measured viral entry based on real-time RT-PCR detection of SARS-CoV mRNA. As shown in Fig. 4*c*, we successfully detected a difference in copy number of the viral mRNA in these cells ($P < 0.01$). The introduction of an *ACE2* siRNA also reduced the copy number of SARS-CoV mRNA (Fig. 4*e*), indicating that this method actually detects viral infection via ACE2. In addition, *TACE* siRNA reduced SARS-CoV infection, indicating that TACE plays an important role in the entry of SARS-CoV. Consistent with these data, TAPI-0, a TACE inhibitor, specifically inhibited the entry of SARS-S (Fig. S4). In addition, although ΔTMC-ACE2 was defective in terms of viral infection, it restored receptor function when TACE was activated by addition of PMA (Fig. S5).

It is unclear how TACE facilitates viral entry. Our observations indicated that the TACE requirement is stronger for SARS-S than for NL63-S (Fig. 5*d*). Recent studies, using peptidases and their inhibitors, suggested that SARS-S is processed in a stepwise fashion (21, 22). Peptidase inhibitors of cathepsin L (23) or Ben·HCl (24) blocked viral infection, whereas the addition of cathepsin L or Factor Xa enhanced viral infection (23–25). The peptidase activity of cathepsin L, which is critical for the fusion of viral particles and cytoplasmic membranes, depends on a low endosomal pH (26). Interestingly, SARS-CoV depends on both cathepsin L (25) and a low endosomal pH (26), whereas HNL63-CoV (25) does not, indicating a possible functional link between TACE and the components required for fusion of viral and plasma membranes.

Because the shed form of ACE2 is catalytically active (Figs. 1–3) and would counteract ACE-induced cellular signals, it is debatable whether ACE2 shedding by itself is a key event leading to tissue damage. It is plausible that prolonged low-level expression of ACE2 is required for the up-regulation of ACE activity in tissue injury. Although it is important to characterize the temporal changes in ACE2 expression after shedding, the results of the present study suggest that the cytoplasmic tail of ACE2 and a cellular response triggered by the interaction between ACE2 and SARS-S are candidate targets for anti-SARS-CoV therapeutics.

Materials and Methods

Cell Culture and Chemicals. Vero E6, HEK293T, and Huh-7 cells were obtained from the Riken BRC Cell Bank. These cells and NIH 3T3 cells were maintained in

Dulbecco's modified Eagle's medium supplemented with 10% FCS. *tace*-KO cells (16) were provided by R. A. Black (Amgen) and maintained in Ham's F-12 supplemented with 2% FCS. Phorbol-12-myristate-13-acetate (PMA) (Sigma) was used as a positive control for ACE2 shedding.

Plasmid Construction. Plasmids encoding full-length hACE2 (4) and residues 12–672 (27) of SARS-S were provided by H. Choe (Harvard Medical School, Boston, MA). Plasmid DNAs encoding the ACE2 mutants or part of SARS-S were constructed by using PCR-based techniques. Each mutant was confirmed by sequencing.

Preparation and Infection of SARS-S and NL63-S. Pseudotyped lentiviruses were prepared as described in ref. 28. HEK293T cells were cotransfected with HIV-1-based lentiviral DNA and plasmids encoding full-length SARS-S (G. J. Nabel, National Institutes of Health, Bethesda, MA) (26), NL63-S (S. Pöhlmann, Friedrich Alexander University of Erlangen–Nuremberg, Erlangen, Germany) (8, 9), or VSV-G (29). p24 of gag protein was measured by using a Retro-Tek HIV-1 p24 ELISA Kit (ZeptoMetrix) in accordance with the manufacturer's instructions. ACE2-expressing HEK293T cells were infected with 100 ng/ml p24 in SARS-S. After 4 h (before integration of the lentiviral DNA into the host genome) (C. N.-M., unpublished data), the cells were treated with trypsin-EDTA to degrade all unincorporated virus.

siRNA and Protein Analyses. siRNAs against *ACE2*, *ADAM10*, and *TACE* were purchased from Ambion and transfected by using Oligofectamine Reagent (Invitrogen) in accordance with the manufacturer's instructions. The sequences are summarized in Fig. S7. The cells were assayed 48 h after transfection.

Monoclonal antibodies against the ACE2 ectodomain (R&D Systems) and polyclonal antibodies against the cytoplasmic tail of TACE (Chemicon), ADAM9 (Santa Cruz Biotechnology), ADAM10 (Chemicon), and β-tubulin (loading control) (NeoMarker) were used for Western blot analysis. Rabbit polyclonal antibodies against the ACE2 cytoplasmic domain were produced by MBL Corp. To examine ACE2 shedding, cells were treated with SARS-S, and the culture supernatants were precipitated with trichloroacetic acid (TCA). As a control, 10 μg of ovalbumin (OVA) was added to each sample and the recovered precipitates were probed with anti-OVA antibodies (Chemicon).

Real-Time PCR Analysis of SARS-CoV mRNA Expression. HEK293T cells or Huh-7 cells in 24-well plates were infected with SARS-CoV FFM-1 strain at an MOI of 1. Four hours after infection, total RNA was purified by ISOGEN (NIPPONGENE). For quantification of SARS-CoV RNA, real time RT-PCR was performed. As a loading control for normalization, 18S ribosomal RNA was quantified. Primers and probes used in the analysis were summarized in Fig. S6. For all of quantification, a one-step RT-PCR kit (Applied Biosystems) was used and the fluorescence intensity generated from the probe was detected by ABI-7700 sequence detector system (Applied Biosystems).

ACE2 Activity Assay. The enzymatic activity of ACE2 was assayed by using 10 μM 7-methoxycoumarin-YVADAPK (2,4-dinitrophenyl)-OH (R&D Systems) as a fluorogenic substrate. Fluorescence was monitored at an excitation wavelength of 320 nm and an emission wavelength of 450 nm.

FACS Analysis. SARS-S was expressed as a chimeric protein with IgG-Fc, using pAB61 (S. Pöhlmann). 293FS cells (Invitrogen) were used for protein expression. The recombinant protein was purified by using G-agarose beads (GE Healthcare). Cells expressing WT-ACE2 or ΔTMC-ACE2 were incubated with the Fc-SARS-S protein, and the bound SARS-S was detected by using FITC-labeled α-IgG.

Solid-Phase Assay to Detect the Binding of SARS-S and ACE2. Recombinant SARS-S and glyceraldehyde dehydrogenase (GAPDH) were expressed and purified by using a pET vector system (Novagen). ACE2 was partially purified from the supernatants of cultured ACE2-expressing 293FS cells by DEAE column chromatography. ELISA plates (Nunc) were coated with viral mutants, and protein and ACE2 was reacted. After incubation α-ACE2 labeled with Alexa Fluor 555 (Molecular Probes), the bound ACE2 was detected by measuring the fluorescence, using Safire 2 (Tecan).

TNF-α Production Assay. TNF-α production was measured by using a human TNF-α ELISA Kit (R&D Systems) in accordance with the manufacturer's instructions.

Statistical Analysis. Statistical significance was evaluated by using Student's *t* test based on triplicate samples unless otherwise stated.

ACKNOWLEDGMENTS. We thank Drs. R. A. Black, H. Choe, G. J. Nabel, S. Pöhlmann, E. W. Raines (University of Washington, Seattle), A. Zolkiewska (University of Kansas, Lawrence), and R. Postina (Johannes Gutenberg University, Mainz, Germany) for providing the *tace*-KO cells and plasmid DNAs encoding *ACE2*, *SARS-S*, *NL63-S*/pAB61, mouse *TACE*, mouse *ADAM9*, and bovine *ADAM10*, respectively. We thank Mr. Y. Okudaira and Ms. S. Nakano for technical assistance. This work was supported by Grants-in-Aid for Research on Emerging and Re-Emerging Infectious Diseases from the Ministry of Health, Labor, and Welfare of Japan and the National Institute of Biomedical Innovation.

1. Kaiazek TG *et al.* (2003) A novel coronavirus associated with severe acute respiratory syndrome. *N Engl J Med* 15:1953–1966.
2. Tipnis SR, *et al.* (2000) A human homolog of angiotensin-converting enzyme. Cloning and functional expression as a captopril-insensitive carboxypeptidase. *J Biol Chem* 275:33238–33243.
3. Nicholls J, Peiris M (2005) Good ACE, bad ACE do battle in lung injury, SARS. *Nat Med* 11:821–822.
4. Li W, *et al.* (2003) Angiotensin-converting enzyme 2 is a functional receptor for the SARS coronavirus. *Nature* 426:450–454.
5. Kuba K, *et al.* (2005) A crucial role of angiotensin converting enzyme 2 (ACE2) in SARS coronavirus-induced lung injury. *Nat Med* 11:875–879.
6. Imai Y, *et al.* (2005) Angiotensin-converting enzyme 2 protects from severe acute lung failure. *Nature* 436:112–116.
7. van der Hoek L, *et al.* (2004) Identification of a new human coronavirus. *Nat Med* 10:368–373.
8. Hofmann H, *et al.* (2005) Human coronavirus NL63 employs the severe acute respiratory syndrome coronavirus receptor for cellular entry. *Proc Natl Acad Sci USA* 102:7988–7993.
9. Hofmann H, *et al.* (2006) Highly conserved regions within the spike proteins of human coronaviruses 229E and NL63 determine recognition of their respective cellular receptors. *J Virol* 80:8639–8652.
10. van der Hoek L, Pyrc K, Berkhout B (2006) Human coronavirus NL63, a new respiratory virus. *FEMS Microbiol Rev* 30:760–773.
11. Yeager CL, *et al.* (1992) Human aminopeptidase N is a receptor for human coronavirus 229E. *Nature* 357:420–422.
12. Black RA, *et al.* (1997) A metalloproteinase disintegrin that releases tumour-necrosis factor-α from cells. *Nature* 385:729–733.
13. Seals DF, Courtneidge SA (2003) The ADAMs family of metalloproteases: Multidomain proteins with multiple functions. *Genes Dev* 17:7–30.
14. Lambert DW, *et al.* (2005) Tumor necrosis factor-α convertase (ADAM17) mediates regulated ectodomain shedding of the severe-acute respiratory syndrome-coronavirus (SARS-CoV) receptor, angiotensin-converting enzyme-2 (ACE2). *J Biol Chem* 280:30113–30119.
15. Mohler KM, *et al.* (1994) Protection against a lethal dose of endotoxin by an inhibitor of tumour necrosis factor processing. *Nature* 370:218–220.
16. Reddy P, *et al.* (2000) Functional analysis of the domain structure of tumor necrosis factor-alpha converting enzyme. *J Biol Chem* 275:14608–14614.
17. Simmons G, *et al.* (2004) Characterization of severe acute respiratory syndrome-associated coronavirus (SARS-CoV) spike glycoprotein-mediated viral entry. *Proc Natl Acad Sci USA* 101:4240–4245.
18. Hofmann H, *et al.* (2004) Susceptibility to SARS coronavirus S protein-driven infection correlates with expression of angiotensin converting enzyme 2 and infection can be blocked by soluble receptor. *Biochem Biophys Res Commun* 319:1216–1221.
19. Gschwendt M, *et al.* (1994) Rottlerin, a novel protein kinase inhibitor. *Biochem Biophys Res Commun* 199:93–98.
20. Inoue Y, *et al.* (2007) Clathrin-dependent entry of severe acute respiratory syndrome coronavirus into target cells expressing ACE2 with the cytoplasmic tail deleted. *J Virol* 81:8722–8729.
21. Liu S, *et al.* (2004) Interaction between heptad repeat 1 and 2 regions in spike protein of SARS-associated coronavirus: Implications for virus fusogenic mechanism and identification of fusion inhibitors. *Lancet* 363:938–947.
22. Wu XD, *et al.* (2004) The spike protein of severe acute respiratory syndrome (SARS) is cleaved in virus infected Vero-E6 cells. *Cell Res* 14:400–406.
23. Simmons G, *et al.* (2005) Inhibitors of cathepsin L prevent severe acute respiratory syndrome coronavirus entry. *Proc Natl Acad Sci USA* 102:11876–11881.
24. Du L, *et al.* (2007) Cleavage of spike protein of SARS coronavirus by protease factor Xa is associated with viral infectivity. *Biochem Biophys Res Commun* 359:174–179.
25. Huang IC, *et al.* (2006) SARS coronavirus, but not human coronavirus NL63, utilizes cathepsin L to infect ACE2-expressing cells. *J Biol Chem* 281:3198–3203.
26. Yang ZY, *et al.* (2004) pH-dependent entry of severe acute respiratory syndrome coronavirus is mediated by the spike glycoprotein and enhanced by dendritic cell transfer through DC-SIGN. *J Virol* 78:5642–5650.
27. Wong SK, Li W, Moore MJ, Choe H, Farzan M (2004) A 193-amino acid fragment of the SARS coronavirus S protein efficiently binds angiotensin-converting enzyme 2. *J Biol Chem* 279:3197–3201.
28. Nakai-Murakami C, *et al.* (2007) HIV-1 Vpr induces ATM-dependent cellular signal with enhanced homologous recombination. *Oncogene* 26:477–486.
29. Tachiwana H, *et al.* (2006) HIV-1 Vpr induces DNA double-strand breaks. *Cancer Res* 66:627–631.

Available online at www.sciencedirect.com
ScienceDirect
Virology 375 (2008) 130–140
VIROLOGY
www.elsevier.com/locate/yviro

Ezrin, Radixin, and Moesin (ERM) proteins function as pleiotropic regulators of human immunodeficiency virus type 1 infection

Yoshinao Kubo [a,*], Hiroaki Yoshii [a], Haruka Kamiyama [a], Chika Tominaga [a], Yuetsu Tanaka [b], Hironori Sato [a,c], Naoki Yamamoto [a,d]

[a] Department of AIDS Research, Institute of Tropical Medicine, Nagasaki University, Nagasaki, National Institute of Infectious Diseases, Tokyo, Japan
[b] Department of Immunology, University of the Ryukyus, Okinawa, National Institute of Infectious Diseases, Tokyo, Japan
[c] Laboratory of Viral Genomics, Center for Pathogen Genomics, National Institute of Infectious Diseases, Tokyo, Japan
[d] AIDS Research Center, National Institute of Infectious Diseases, Tokyo, Japan

Received 5 November 2007; returned to author for revision 21 November 2007; accepted 30 January 2008
Available online 4 March 2008

Abstract

Ezrin, radixin, and moesin (ERM) proteins supply functional linkage between integral membrane proteins and cytoskeleton in mammalian cells to regulate membrane protein dynamisms and cytoskeleton rearrangement. To assess potential role of the ERM proteins in HIV-1 lifecycle, we examined if suppression of ERM function in human cells expressing HIV-1 infection receptors influences HIV-1 envelope (Env)-mediated HIV-1-vector transduction and cell–cell fusion. Expression of an ezrin dominant negative mutant or knockdown of ezrin, radixin, or moesin with siRNA uniformly decreased transduction titers of HIV-1 vectors having X4-tropic Env. In contrast, transduction titers of R5-tropic Env HIV-1 vectors were decreased only by radixin knockdown: ezrin knockdown had no detectable effects and moesin knockdown rather increased transduction titer. Each of the ERM suppressions had no detectable effects on cell surface expression of CD4, CCR5, and CXCR4 or VSV-Env-mediated HIV-1 vector transductions. Finally, the individual knockdown of ERM mRNAs uniformly decreased efficiency of cell–cell fusion mediated by X4- or R5-tropic Env and HIV-1 infection receptors. These results suggest that (i) the ERM proteins function as positive regulators of infection by X4-tropic HIV-1, (ii) moesin additionally functions as a negative regulator of R5-tropic HIV-1 virus infection at the early step(s) after the membrane fusion, and (iii) receptor protein dynamisms are regulated differently in R5- and X4-tropic HIV-1 infections.

Keywords: HIV-1; Ezrin; Radixin; Moesin

Introduction

Human immunodeficiency virus type 1 (HIV-1) enters into host cells by fusion between viral envelope and host cell membrane following the binding of HIV-1 envelope glycoprotein (Env) to the cell surface receptors, CD4 and co-receptor (CXCR4 or CCR5). The HIV-1 Env glycoprotein is synthesized as a precursor polyprotein, and cleaved to surface (SU) and transmembrane (TM) subunits by a cellular protease. The conformational change of SU subunit by its interaction with CD4 triggers the formation and exposure of the co-receptor binding domain. The binding of SU subunit to the co-receptor molecule activates the membrane fusion capability of the viral TM subunit required for the HIV-1 entry into host cells.

After the HIV-1 Env protein binds to host cells, the HIV-1 infection receptors are clustered (Jolly and Sattentau, 2005; Nguyen et al., 2005; Viard et al., 2002). The receptor clustering requires cytoskeletal functions (Iyengar et al., 1998; Jolly et al., 2004; Kizhatil and Albritton, 1997; Lehmann et al., 2005; Pontow et al., 2004; Steffens and Hope, 2003). This results in multiple interactions between the viral Env proteins and the host receptor molecules on the interacting site between host cell and virion (Jimenez-Baranda et al., 2007; Platt et al., 1998). Although accumulating evidence indicates that the cytoskeleton-dependent clustering of infection receptors are essential for

* Corresponding author. Department of AIDS Research, Institute of Tropical Medicine, Nagasaki University, 1-12-4 Sakamoto, Nagasaki, Japan 852-8523. Fax: +81 95 849 7805.
E-mail address: yoshinao@net.nagasaki-u.ac.jp (Y. Kubo).

0042-6822/$ - see front matter © 2008 Elsevier Inc. All rights reserved.
doi:10.1016/j.virol.2008.01.047

efficient membrane fusion and subsequent entry of HIV-1 into the target cells, there is no evidence that the receptor proteins, CD4, CXCR4, and CCR5, directly bind to the cytoskeleton. This suggests that some linker molecules between the receptor and cytoskeleton is involved in the HIV-1 entry.

Ezrin, radixin, and moesin are the cytosolic proteins called ERM family that supplies functional linkage between integral membrane proteins and cytoskeleton (Algrain et al., 1993; Fievet et al., 2006; Tsukita et al., 1997). They are highly homologous each other, sharing about 70–80% amino acid identity. The ERM plays key roles in cell morphogenesis and communication via regulating membrane protein dynamisms and cytoskeleton rearrangement (Tsukita et al., 1997). The ERM, particularly ezrin, is important for reconstructing cell-surface architecture during T cell activation (Das et al., 2002; Faure et al., 2004; Gupta et al., 2006; Roumier et al., 2001). Despite the general similarity in structure and function, individual function of the three proteins appears to be specialized (Doi et al., 1999; Kikuchi et al., 2002; Saotome et al., 2004; Takeuchi et al., 1994). Ezrin is crucial for formation of local architecture, called immunological synapse, at the contact site of antigen-presenting and T cells (Gupta et al., 2006; Roumier et al., 2001). Dephosphorylation and relocation of

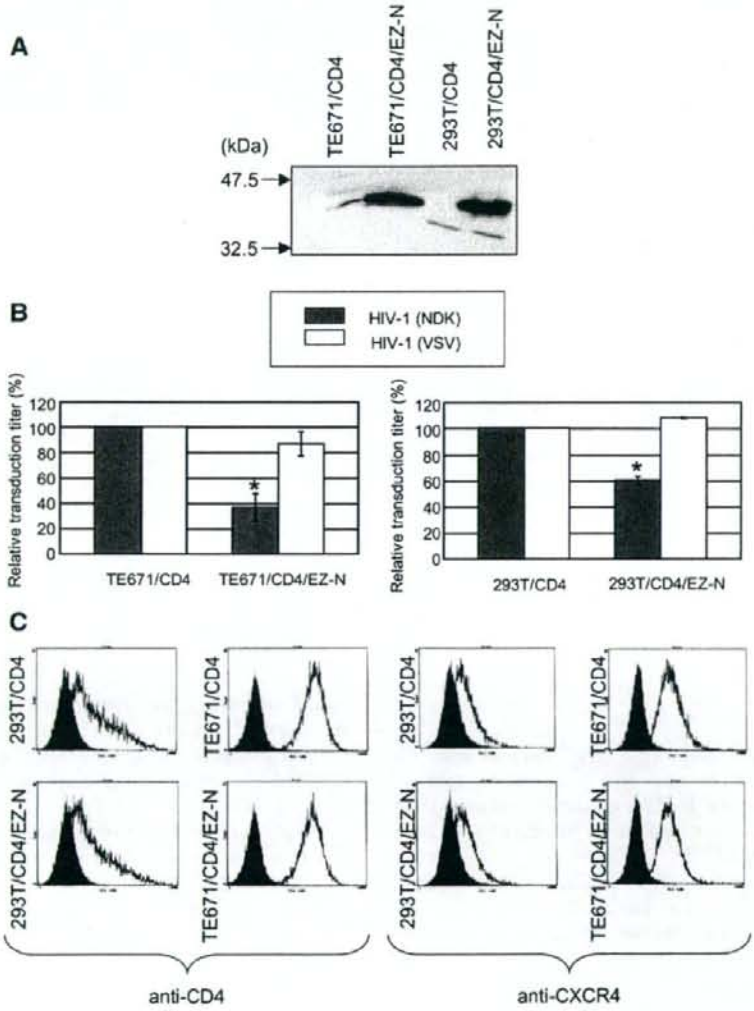

Fig. 1. Effect of ezrin dominant negative mutant on vector transduction. Panel A. Cell lysates prepared from cells expressing the VSV-G epitope-tagged ezrin dominant negative mutant (EZ-N) were subjected to Western immunoblotting using the anti-VSV-G epitope antibody. Molecular size markers are indicated in left side of the panel. Panel B. Transduction titers of the HIV-1 vector having VSV-G (open bar) or NDK HIV-1 Env (closed bar) protein were measured in the control and EZ-N-expressing cells. Relative values to the titer in the control cells are shown. Three independent experiments were performed. Error bars indicate standard deviations. Panel C. Cell surface expression of CD4 and CXCR4 in the control and the EZ-N-expressing cells was analysed by FACS. Closed areas indicate cells stained without the first antibody. Open areas indicate cells stained with the anti-CD4 or anti-CXCR4 antibody.

ezrin trigger transient uncoupling of lipid rafts or plasma membrane from the actin cytoskeleton, which presumably increases lipid raft dynamics and T cell receptor clustering (Gupta et al., 2006). The immunological synapse contains CD4 and CXCR4 (Roumier et al., 2001), the HIV-1 infection receptors, and its formation requires cytoskeleton rearrangement (Das et al., 2002). In addition, the HIV-1 receptors have been reported to co-localize with ezrin (Steffens and Hope, 2003).

In this study, we examined potential roles of the ERM proteins in the HIV-1 infection. We prepared HIV-1-susceptible human cells in which function or expression of the ERM family proteins were suppressed by either ezrin dominant negative mutant (Algrain et al., 1993) or by RNA interference technique (Rana, 2007). Suppression of individual ERM in the target cells yielded distinct effects on HIV-1 vector transductions mediated by the X4- and R5-tropic Env proteins. The ERM suppressions uniformly inhibited cell–cell fusion mediated by the X4- and R5-tropic envelope proteins. Our findings provide for the first time the evidence that the ERM family proteins function as pleiotropic regulators of HIV-1 infection.

Results

Ezrin dominant negative mutant inhibits X4-tropic HIV-1 vector infection

The N-terminal and C-terminal domains of ezrin bind membrane proteins and cytoskeleton, respectively (Tsukita et al., 1997). Expression of an ezrin N-terminal domain has been reported to interfere with the endogenous ezrin function as a dominant negative mutant (Algrain et al., 1993; Roumier et al., 2001). To examine if the ezrin influences HIV-1 infection, we prepared human cells expressing the ezrin dominant negative mutant (EZ-N) that is C-terminally tagged with the VSV-G epitope (Algrain et al., 1993). A murine leukemia virus (MLV) vector carrying the EZ-N was inoculated into 293T and TE671 cells expressing CD4 (293T/CD4 and TE671/CD4), and the cells were selected by puromycin. Because the MLV vector genome contained both of the EZ-N and puromycin-resistant genes, it was thought that almost all of the puromycin-resistant cells expressed the EZ-N protein. Western immunoblotting using the anti-VSV-G epitope antibody indicates that the puromycin-resistant cell pools expressed the VSV-G-tagged EZ-N protein as the predicted size (Fig. 1A).

The parental TE671/CD4 and 293T/CD4 cells were susceptible to HIV-1 vector having the X4-tropic NDK HIV-1 Env protein, because the cells endogenously express CXCR4. Transduction titers of the HIV-1 NDK Env vector in TE671/CD4 and 293T/CD4 cells expressing the EZ-N were constantly decreased (Fig. 1B). Such reduction in virus titer was observed when HIV-1 vector having Env protein of a CD4-independent X4-tropic virus strain, mNDK (Dumonceaux et al., 1998), was used as a transduction source (data not shown). In contrast, the EZ-N expression had little effects on the infection of HIV-1 vector having VSV-G protein. Expression of the EZ-N had little effects on cell surface expression of the HIV-1 receptors, CD4 and CXCR4, as monitored by FACS analysis (Fig. 1C). These results suggest that ezrin functions as a positive regulator of HIV-1 infection mediated by the X4-tropic HIV-1 Env but not by the VSV-Env.

To assess whether the EZ-N affects R5-tropic HIV-1 vector transduction, transduction titers of the HIV-1 vector having the R5-tropic JRFL HIV-1 Env protein were measured in target cells transiently transfected with the VSV-G-tagged wild type ezrin (EZ-Wt) or the EZ-N expression plasmid. TE671 cells expressing CD4 and CCR5 (TE671/CD4/R5) were used as the target cells. The EZ-N reduced transduction titer of the X4-tropic NDK HIV-1 vector in the TE671/CD4/R5 cells (Fig. 2A)

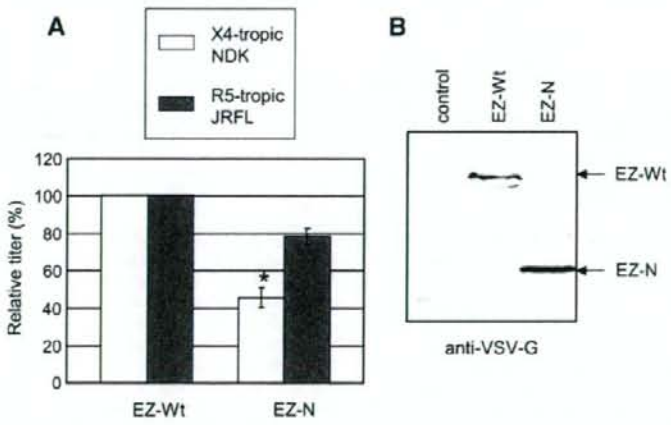

Fig. 2. Effect of ezrin dominant negative mutant on R5-tropic HIV-1 vector transduction. Panel A. Transduction titers of the HIV-1 vector having the X4-tropic NDK (open bar) or R5-tropic JRFL (closed bar) Env protein were measured in TE671/CD4/R5 cells transiently transfected with the wild type ezrin (EZ-Wt) or ezrin dominant negative mutant (EZ-N) expression plasmid. Relative titers to that in the EZ-Wt-transfected cells were indicated. This experiment was repeated three times, and error bars indicate standard deviations. Panel B. Western immunoblotting of the transfected cells was performed using the anti-VSV-G epitope antibody. The EZ-Wt and EZ-N proteins are estimated by their molecular sizes, and are shown by arrows.